

Ambient and Elevated Temperature Fracture and Cyclic-Fatigue Properties in a Series
of Al-Containing Silicon Carbide Ceramics

by

Rong Yuan

B.S. (Tsinghua University, Beijing, China) 1999

A thesis submitted in partial satisfaction of the
requirements for the degree of

Master of Science

in

Engineering: Materials Science and Engineering

in the

GRADUATE DIVISION

of the

UNIVERSITY OF CALIFORNIA, BERKELEY

Committee in charge:

Professor Robert O. Ritchie, Chair
Professor Lutgard C. De Jonghe
Professor Panos Papadopoulos

2004

Abstract

Ambient and Elevated Temperature Fracture and Cyclic-Fatigue Properties of a Series of Al-containing Silicon Carbides

By
Rong Yuan

Master of Science in Materials Science and Engineering
University of California, Berkeley
Professor R. O. Ritchie, Chair

Abstract—A series of *in situ* toughened, Al, B and C containing, silicon carbide ceramics (ABC-SiC) has been examined with Al contents varying from 3 to 7 wt%. With increasing Al additions, the grain morphology in the as-processed microstructures varied from elongated to bimodal to equiaxed, with a change in the nature of the grain-boundary film from amorphous to partially crystalline to fully crystalline. Fracture toughness and cyclic fatigue tests on these microstructures revealed that although the 7 wt.% Al containing material (7ABC) was extremely brittle, the 3 and particularly 5 wt.% Al materials (3ABC and 5ABC, respectively) displayed excellent crack-growth resistance at both ambient (25°C) and elevated (1300°C) temperatures. Indeed, no evidence of creep damage, in the form of grain-boundary cavitation, was seen at temperatures at 1300°C or below. The enhanced toughness of the higher Al-containing materials was associated with extensive crack bridging from both interlocking grains (in 3ABC) and uncracked ligaments (in 5ABC); in contrast, the 7ABC SiC showed no such bridging, concomitant with a marked reduction in the volume fraction of elongated grains. Mechanistically, cyclic fatigue-crack growth in 3ABC and 5ABC SiC involved the progressive degradation of such bridging ligaments in the crack wake, with the difference in the

degree of elastic vs. frictional bridging affecting the slope, i.e., Paris law exponent, of the crack-growth curve.

In addition an investigation of fracture resistance in non-transforming ceramics toughened by grain bridging mechanism is presented using linear elastic fracture mechanics (LEFM). Linear superposition theorems are used for the superposition of crack opening displacements, as well as stress intensity factors, resulting from the external tractions and the internal compressive bridging stresses. Specifically weight functions are used to relate the CODs, stress intensity factors, and tractions and the bridging stress. Expressions are derived for apparent material resistance, the bridging resistance and the intrinsic toughness, and an experimental procedure is proposed by which these predictions can be verified. .

TABLE OF CONTENTS

| | |
|---|-----|
| List of Figures | iv |
| List of Tables | vi |
| Acknowledgements | vii |
| | |
| Chapter 1: Background and Objectives | 1 |
| 1.1 Synopsis | 1 |
| 1.2 Materials in Study..... | 2 |
| 1.2.1 Crystallographic and Structural Properties of SiC | 2 |
| 1.2.2 ABC-SiC | 3 |
| 1.3 Objectives of the Present Work | 5 |
| References | 6 |
| Figures..... | 7 |
| | |
| Chapter 2: Ambient to High-Temperature Fracture Toughness and Cyclic-Fatigue Behavior in Al-containing silicon carbide ceramics..... | 8 |
| 2.1 Experimental Procedures | 8 |
| 2.1.1 Materials Processing | 8 |
| 2.1.2 Microstructure Characterization | 9 |
| 2.1.3 Fracture and Fatigue testing..... | 10 |
| 2.1.3.1 R-curve test..... | 10 |
| 2.1.3.2 Cyclic Fatigue test at room temperature | 11 |

| | |
|--|--------|
| 2.1.3.3 Cyclic Fatigue Crack Growth at high temperature | 12 |
| 2.1.4 Fractography | 12 |
| 2.1.5 Crack-Opening Profile Measurements..... | 13 |
| 2.2 Results..... | 13 |
| 2.2.1 Microstructure Features | 13 |
| 2.2.1.1 Phase and Grain Morphology | 13 |
| 2.2.1.2 Grain Boundaries | 14 |
| 2.2.2 Fracture Toughness and Strength..... | 16 |
| 2.2.2.1 Fracture Toughness | 16 |
| 2.2.2.2 Strength..... | 16 |
| 2.2.3 Fatigue-Crack Growth Behavior | 17 |
| 2.2.4 Fractography and Crack Paths | 18 |
| 2.2.5 Crack Opening Profile Results..... | 19 |
| 2.3 Discussion..... | 21 |
| 2.3.1 Toughening Mechanism..... | 21 |
| 2.3.2 Cyclic Fatigue Mechanism | 24 |
| 2.4 Conclusions | 25 |
| Appendix 2.1 | 27 |
| References..... | 29 |
| Figures..... | 30 |
| Chapter 3: A GRAIN BRIDGING MODEL FOR NONTRANSFORMING CERAMICS | 40 |
| 3.1 REVIEW OF GRAIN BRIDGING MODEL | 40 |
| 3.1.1 Microstructural Aspects..... | 41 |

| | |
|---|----|
| 3.1.1.1 Bridging Forms and Micromechanics Constitutive Law | 41 |
| 3.1.1.2 Physical Origin of the bridging stress | 43 |
| 3.1.1.3 The Effects of Microstructure on Bridging Stress and R-curve | 43 |
| 3.1.2 Quantification of Bridging Stress and R-curve Behavior | 44 |
| 3.1.2.1 Integral of the bridging stress by LEFM | 45 |
| 3.1.2.2 Compliance Cutting | 46 |
| 3.1.2.3 J-integral by Steinbrech | 46 |
| 3.1.2.4 Post Fracture Tensile Test (PFT) | 47 |
| 3.1.2.5 work loop combined with a frictional bridging model | 48 |
| 3.2 GRAIN BRIDGING MODEL BY LEFM | 48 |
| 3.2.1 Prerequisites | 49 |
| 3.2.2 Critical Crack Driving Force and the Material Resistance | 51 |
| 3.2.3 Proposed experimental procedure to obtain the material resistance and the stress intensity factors | 53 |
| 3.2.4 Discussion | 54 |
| 3.3 CONCLUSIONS | 55 |
| Appendix 3.1 Weight Function and Barenblatt Relation | 57 |
| Appendix 3.2 Actual Work and Virtual Work | 59 |
| References | 62 |
| Figures | 64 |
| Chapter 4: SUMMERY AND FUTURE WORK | 74 |

LIST OF FIGURES

Figure 1.1: Figure 1-1: (a) Crystal structures and (b) stacking sequence for various SiC polytypes [16].

Fig. 2.1. SEM micrographs of etched surfaces of ABC-silicon carbides, showing the characteristic grain structures: (a) uniformly elongated grains in 3ABC, (b) bimodal structure of elongated (α -SiC) and equiaxed (β -SiC) in 5ABC, and (c) equiaxed grains with sparsely distributed needle-like grains in 7ABC. (Courtesy of Qing Yang)

Fig. 2.2. High-resolution TEM micrographs showing the nature of the grain-boundary films in hot-pressed SiC with different Al content, showing (a) amorphous films in 3ABC, (b) fully crystallized films in 7ABC, and (c) amorphous, (d) partially crystallized and (e) fully crystallized films in 5ABC. (Courtesy of Dr. Xiao-Feng Zhang)

Fig. 2.3. Crack growth resistance, K_R , plotted as a function of crack extension, Δa , for as-hot-pressed and annealed xABC-SiC at room temperature.

Fig. 2.4. Cyclic fatigue-crack growth rates, da/dN , at $R = 0.1$ in ABC-SiC, as a function of the applied stress-intensity range, ΔK , at temperatures of 25° and 1300°C. Note that 7ABC is sufficiently brittle that it exhibits no subcritical crack growth, i.e., it fails catastrophically once $K_{\max} > K_c$; the dashed curve for this structure is drawn where $K_{\text{th,max}} = K_c$.

Fig. 2.5. SEM micrographs of the overload fracture surfaces of (a) 3ABC-, (b) 5ABC- and (c) 7ABC-SiC. Fracture in 3ABC and 5ABC is intergranular, whereas it is predominantly transgranular in 7ABC.

Fig. 2.6. SEM micrographs of metallographic sections taken perpendicular to the fracture surface showing the crack paths during fatigue-crack growth at 25°C and 1300°C for 3ABC (a,b) and 5ABC-SiC (c-f). Frictional bridging (a,b,f) was most common in 3ABC while uncracked ligament bridges (c,d,e) were predominant in 5ABC. The horizontal arrows indicate the general direction of crack growth.

Fig. 2.7. Transmission electron micrographs near the crack tip in (a) 3ABC, and (b, c) 5ABC grown under cyclic loading at 1300°C ($R = 0.1$, $\nu = 25$ Hz). Note in (b) the equiaxed grains also fracture intergranularly and in (c) a failure of uncracked ligament. Large arrows indicate the general direction of crack propagation, and small arrows point to the primary cracks near the crack tip. (Courtesy of Dr. Xiao-Feng Zhang)

Fig. 2.8. Comparison of the crack-opening profiles for a monotonically-loaded crack in the 3ABC and 5ABC microstructure after R-curve testing. Samples were loaded *in situ* in a field-emission FESEM to an applied driving force of 6.2 MPa $\sqrt{\text{m}}$. The inset shows the curve fit for the first 70 μm behind the crack tip, where the solid line is for 5ABC ($K_{\text{tip}}=1.6$ MPa $\sqrt{\text{m}}$), and the broken line for 3ABC ($K_{\text{tip}}=2.5$ MPa $\sqrt{\text{m}}$).

Fig. 2.9. Schematic illustrations of how the crack paths lead to the development (or not) of crack bridging in (a) 3ABC, (b) 5ABC, and (c) 7ABC-SiC. Note how the predominant mode of bridging in 3ABC is from frictional grain bridging, whereas it results more from uncracked ligaments in 5ABC; in contrast, no bridging is developed in the 7ABC. (Courtesy of Prof. De Jonghe).

Fig. 3.1 Fig. 3.1 Translation of the bridging stress with crack growth, based on Figure 2 in Ref. [4].

Fig. 3.2. Linear superposition for crack opening displacements u and stress intensity factors K in the grain bridging model. The crack openings are exaggerated.

Fig. 3.3 The relationship among loading on boundary, the resultant displacements, the stress intensity factors and the material resistance in a quasi-static crack propagation process in linear elastic material. The loading, stress intensity factors, and the displacements are related by the weight function in LEFM; furthermore, the material resistance is derived from the virtual work calculated from the loading and the resultant displacements. However, the relationship between material resistance and the stress intensity factor is unknown.

Fig. 3.4. Virtual work caused by external traction and internal compressive bridging stress is evaluated on the boundary of the specimen, where the crack faces are part of the boundary.

Fig. 3.5 Illustration of the experimental procedures to obtain the material resistance and the stress intensity factors. a) ASTM specimens; b) data collection from experiments: load, P , load-point displacement, δ , and the crack size, a ; c) half of the virtual work $vs.$ crack length a ; d) Apparent fracture resistance $vs.$ crack size a ; e) applied stress intensity factor with crack length, a ; f) Intrinsic stress intensity factor from the linear regression fit of $R_A(a)$ and $K_{App}(a)$

Fig. 3.6. Crack opening profiles with crack growth. When $a_0=x$, there is no displacement at x ; when a passes x , the displacement increases with the crack length.

Fig. 3.7 Change of integral sequence to obtain the crack opening displacement from stress distribution along crack surfaces and weight functions. Broken arrows correspond to the integral sequence of the first equation in Eq. (A3.4) and solid ones to the sequence of the second equation in Eq. (A3.4).

Fig. 3.8. At state 1, the actual work is the area OA_1A , virtual work OO_1A_1A ; at state 2, the actual work is the area OB_1B , virtual work OO_2B_1B

Fig. 3.9 The incremental energy for crack growth from a to $a+\delta a$ is indeed the loop of the work done $OA'B'C$, $\mathcal{G}_C(B\delta a)=\delta W-\delta U^{el}$. The equation holds true in elastically unloading materials experiencing a) linear elastic fracture; b) nonlinear elastic fracture; c) linear elastic-plastic fracture.

LIST OF TABLES

Table 2.1. Comparison of Microstructures of ABC-SiC (after Ref. [8])

Table 2.2. Comparison of Mechanical Properties of ABC-SiC

Table 2.3. Cyclic fatigue-crack growth properties for ABC-SiC tested at $R=0.1$, $f=25\text{Hz}$

ACKNOWLEDGEMENTS

First and foremost I would like to thank my family for their love and encouragement to me throughout the rough time. My life would be meaningless without their being happy and contented, so all the good I have done is dedicated to them and the bad kept for myself.

I also greatly appreciate the direction and help from my advisor, Professor Robert O. Ritchie, for providing a positive environment for the work. I would like to thank my group members, Dr. Jay Kruzic, Dr. Jim McNaney, Dr. Heeman Choe, Dr. Alexander Ziegler, Dr. Valentina Imbeni, Dr. Ravi Nalla and Yong Gao for their help and useful discussions through the course of the research. My special respect is due to Dr. Da Chen. He replied my questions about the tests even in his late days fighting with cancer, and his positive attitude towards all the difficulties did affect me much.

The SiC project benefited greatly from the collaboration with Professor Lutgard C. De Jonghe and his research group members. I would like to thank Dr. Xiao-Feng Zhang for the discussion and the beautiful TEM work for this project, and Qing Yang, for preparing a part of the samples for tests.

Professor Papadopoulos, who led me into the world of mechanics and kindly directed me in the study, deserves my heartfelt thanks. I am also deeply grateful to two of my friends, Gang Wang, for the help during the study in mechanics and, and Dah-Wei Chiou, for working with me in his spare time on the program of XRD analysis of SiC.

CHAPTER 1

BACKGROUND AND OBJECTIVES

1.1 SYNOPSIS

Three elements constitute the basis of fracture mechanics: microstructure (materials), testing conditions, and the analytical models through which fracture properties are calculated from the measured quantities in the tests. Different combinations of microstructure and testing conditions require different models to obtain the fracture properties. For example, plasticity is usually considered for metals at ambient temperatures, but not for ceramics; viscoelasticity or viscoplasticity is taken into account for the creep behavior of some materials at high temperatures.

The recent progress in ceramics toughened by the grain bridging mechanism has given rise to renewed interest in such materials since the fracture toughness and the fatigue thresholds have all been increased substantially. Consequently, various characterization techniques have been used to determine the microstructure features which caused such an increase in the toughness [1-3]. Several different analytical models have been proposed to quantify the fracture properties [3-12], and various experimental methods devised and employed to measure the required quantities [2,3,9,12,13]. However, the effect of microstructure on the fracture properties has not been systematically examined, although some researchers have studied the effect of parameters such as grain size and grain size distribution [3,14]). In addition, the analytical models based on linear elastic fracture mechanics (LEFM) that have been used have not always been clearly stated, and in certain cases, the relationship between the stress intensity factor and the material fracture resistance has been incorrect [2,4,8].

Therefore, to address some of these issues, this study will focus on experiments to explore the role of microstructure on the fracture and cyclic fatigue properties at ambient and at elevated temperatures. Additionally, analytical models based on LEFM will be developed to quantify the fracture properties theoretically. The material system for these investigations is a series of aluminum containing silicon carbide ceramics with small additions of boron and carbon (ABC-SiC) [15]. A brief introduction is presented below on the crystallographic and structural properties together with the development of these ABC-SiCs, followed by a statement of the objectives of the current work.

1.2 SILICON CARBIDE CERAMICS

1.2.1 Crystallographic and Structural Properties of SiC

In silicon carbide, four carbon atoms are covalently bonded to a silicon atom and vice versa. It is this strong bonding that imparts to silicon carbide its high compressive strength and modulus, good oxidation resistance and creep resistance, and low density, etc. Due to the very small differences in the stacking fault energy of the close packed planes, silicon carbide exists in a number of forms, which are usually divided into two principal categories: β phase and α phase (Fig. 1.1 [16]). The β phase, a cubic phase, denoted as 3C (Ramsdell notation), has a zinc blende structure, consisting of a series of three repeating layers stacked as $\cdots ABC \cdots$. The grains of β phase often look equiaxed. In contrast, the α phase is composed of hexagonal and rhombohedral phases, among which the most commonly observed are 6H ($\cdots ABCACB \cdots$), 4H ($\cdots ABAC \cdots$) and 2H ($\cdots AB \cdots$). The α phases often grow into large elongated, plate-shaped grains [16]. From the phase diagram, the β phase is usually considered the low temperature phase, whereas the α phase is the stable high-

temperature phase. Once the β phase transforms into one of the α phases at high temperature, the transformed α phase does not revert back.

Since the shape and the morphology of the grains in ceramics play an important role in the toughening mechanisms, specific microstructures need to be developed in sintered ceramics. Consequently, dopants are added, ostensibly to aid sintering, but which can facilitate the growth of the desired phases to produce the desired microstructures that have the optimal fracture resistance properties. In this study, aluminum, boron, and carbon are added to obtain a series of ABC-SiCs with aluminum contents varying from 3 wt% to 7wt%.

1.2.2 ABC-SiC

Silicon carbide (SiC) ceramics represent a class of materials that may potentially replace Ni-base superalloys as higher temperature engine materials because of their high strength, low density and superior oxidation/creep resistance above 1100°C. However, one principal factor which limits their application is their low fracture toughness, which in commercial material is typically on the order of 2-3 MPa \sqrt{m} . In light of this, much of the recent research on SiC [17-27] has focused on ways to increase this toughness. Of these, the approach of *in situ* toughening with aluminum, boron and carbon additions to produce so-called ABC-SiC [19] has been particularly successful in increasing the ambient-temperature fracture toughness to above 9 MPa \sqrt{m} [23], which is believed to be the highest toughness ever reported for SiC. This was achieved in a 3 wt.% Al-containing material (3ABC-SiC) by developing a microstructure of interlocking, high aspect-ratio grains, separated by grain boundaries weakened by the presence of a thin intergranular glassy film; which in turn induced

intergranular fracture and consequent extrinsic toughening¹ from the bridging of interlocking grains in the crack wake [23]. However, under cyclic loading, 3ABC-SiC was found to be susceptible to fatigue-crack growth, due to cyclic-loading induced degradation of the grain bridging zone [23,24].

Subsequent work on 3ABC-SiC at elevated temperatures [25-27,29] revealed that the fracture toughness and fatigue-crack growth properties were only marginally reduced at temperatures of up to 1300°C, with no apparent change in cracking and shielding mechanisms. Furthermore, little or no evidence of creep damage, in the form of grain-boundary cavitation, could be detected at temperatures below 1350°C [29]. This excellent combination of low-temperature toughness and high-temperature toughness/creep behavior was found to be the result of a remarkable property of 3ABC-SiC- that of *in situ* crystallization of the intergranular glassy films at temperatures above ~1100°C [25-27,29,30]. Moreover, although the grain-boundary films remained crystalline, the high toughness was retained, and indeed increased, on subsequently cooling to room temperature [26].

Accordingly, from the perspective of developing SiC with such optimized properties, two means of controlling the microstructure in ABC-SiC can be contemplated. The first involves annealing the material (e.g., at 1300°C) prior to use to cause the crystallization of the amorphous grain-boundary films. Chen *et al.* [25-27] found that in addition to conferring good high-temperature creep and fatigue resistance, such heat treatments led to a ~20% increase in the room-temperature fracture toughness and fatigue-crack growth resistance (with no change in mechanism), compared to that in the as-hot-pressed material. However, an alternative

¹ *Extrinsic* toughening involves micro-mechanisms, such as crack bridging or microcracking, which act primarily in the crack wake to *locally* “shield” the crack from the applied (*global*) driving force; they therefore enhance the crack-growth toughness and invariably result in resistance-curve behavior. They are to be compared with *intrinsic* mechanisms which operate ahead of the crack tip to enhance the inherent toughness of the material; these mechanisms mainly promote resistance to crack initiation [28].

approach is via microstructure modification through compositional changes, specifically by varying the aluminum content [31]. To date, several ABC-SiC materials have been processed with aluminum contents between 3 and 7 wt.%, where the changing Al additions resulted in significantly altered microstructures [23-27,31]. Whereas the 3 wt.% material (3ABC) develops a microstructure of relatively uniform elongated grains with amorphous grain-boundary films (as noted above), a bimodal distribution of both elongated and equiaxed grains with partially crystallized grain-boundary films is seen in the 5ABC material (5 wt.% Al), compared to principally equiaxed grains with only a few elongated (needle-like) grains, all with fully crystallized grain boundaries, in the 7ABC-SiC (7 wt.% Al).

1.3 OBJECTIVES OF THE PRESENT WORK

The focus of this work is to present a detailed examination of the fracture toughness and fatigue properties of three ABC-SiC microstructures from ambient to elevated temperatures (25° to 1300°C), with the objective of defining the salient damage and toughening mechanisms and their relationship to the characteristic microstructures involved. In addition, an effort is made to formulate the relationship between material resistance and the stress intensity factors in the grain bridging model using linear elastic fracture mechanics (LEFM). Finally, a review is presented of developments in the field of grain bridging.

REFERENCES

- [1] Swanson PL, Fairbanks CJ, Lawn BR, Mai Y-W, Hockey BJ. *Journal of American Ceramics Society* 1987;70:279.
- [2] Rodel J, Kelly JF, Lawn BR. *Journal of American Ceramics Society* 1990;73:3313.
- [3] Vekinis G, Ashby MF, Beaumont PWR. *ACTA METALLURGICA ET MATERIALIA* 1990;38:1151.
- [4] Mai Y-W, Lawn BR. *Journal of American Ceramics Society* 1987;70:289.
- [5] Bennison SJ, Lawn BR. *ACTA METALLURGICA* 1989;37:2659.
- [6] Fett T, Munz D. *Journal of American Ceramics Society* 1994;77:3267.
- [7] Fett T, Munz D, Thun G. *Journal of American Ceramics Society* 1995;78:949.
- [8] Steinbrech RW, Reichl A, Schaarwachter W. *Journal of American Ceramics Society* 1990;73:2009.
- [9] Hay JC, White KW. *Acta Metallurgy Materiala* 1992;40:3017.
- [10] Hay JC, White KW. *Journal of American Ceramics Society* 1993;76:1849.
- [11] Hu X-Z, Lutz EH, Swain MV. *Journal of American Ceramics Society* 1991;74:1828.
- [12] Hu X-Z, Wittmann FH. *Cement and Concrete Research* 1991;21:1118.
- [13] Fett T, Munz D, Dai X, White KW. *International Journal of Fracture* 2000;104:375.
- [14] Becher PF, Sun EY, Plucknett KP, Alexander KB, Hsueh C-H, Lin H-T, Waters SB, Westmoreland CG. *Journal of American Ceramics Society* 1998;81:2821.
- [15] Zhang XF, Yang Q, De Jonghe LC. *Acta Materialia* 2003;51:3849.
- [16] Yang Q. Master, University of California, Berkeley, Berkeley, 2001.
- [17] Kim DH, Kim CH. *Journal of the American Ceramic Society* 1990;73:1431.
- [18] Mitchell Jr TD, De Jonghe LC, MoberlyChan WJ, Ritchie RO. *Journal of the American Ceramic Society* 1995;78:97.
- [19] Cao JJ, MoberlyChan WJ, De Jonghe LC, Gilbert CJ, Ritchie RO. *Journal of the American Ceramic Society* 1996;79:461.
- [20] Padture NP. *Journal of the American Ceramic Society* 1994;77:519.
- [21] Padture NP, Lawn BR. *Journal of the American Ceramic Society* 1994;77:2518.
- [22] Lee SK, Kim CH. *Journal of the American Ceramic Society* 1994;77:1655.
- [23] Gilbert CJ, Cao JJ, MoberlyChan WJ, De Jonghe LC, Ritchie RO. *Acta Metallurgica et Materialia* 1996;44:3199.
- [24] Gilbert CJ, Ritchie RO. *Acta Materialia* 1998;46:609.
- [25] Chen D, Gilbert CJ, Zhang XF, Ritchie RO. *Acta Materialia* 2000;48:659.
- [26] Chen D, Zhang XF, Ritchie RO. *Journal of the American Ceramic Society* 2000;83:2079.
- [27] Chen D, Sixta ME, Zhang XF, De Jonghe LC, Ritchie RO. 2000, 4599.
- [28] Ritchie RO. *International Journal of Fracture* 1999;100:55.
- [29] Sixta M, Zhang XF, De Jonghe LC. *Journal of the American Ceramic Society* 2001;84:2022.
- [30] Zhang XF, Sixta M, De Jonghe LC. *Journal of the American Ceramic Society* 2000;83:2813.
- [31] Zhang XF, Yang Q, De Jonghe LC. *Acta Materialia* 2003;51:3849.

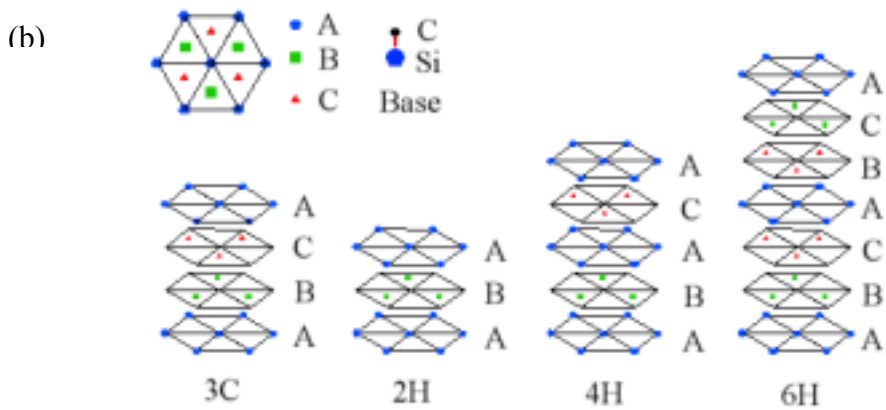
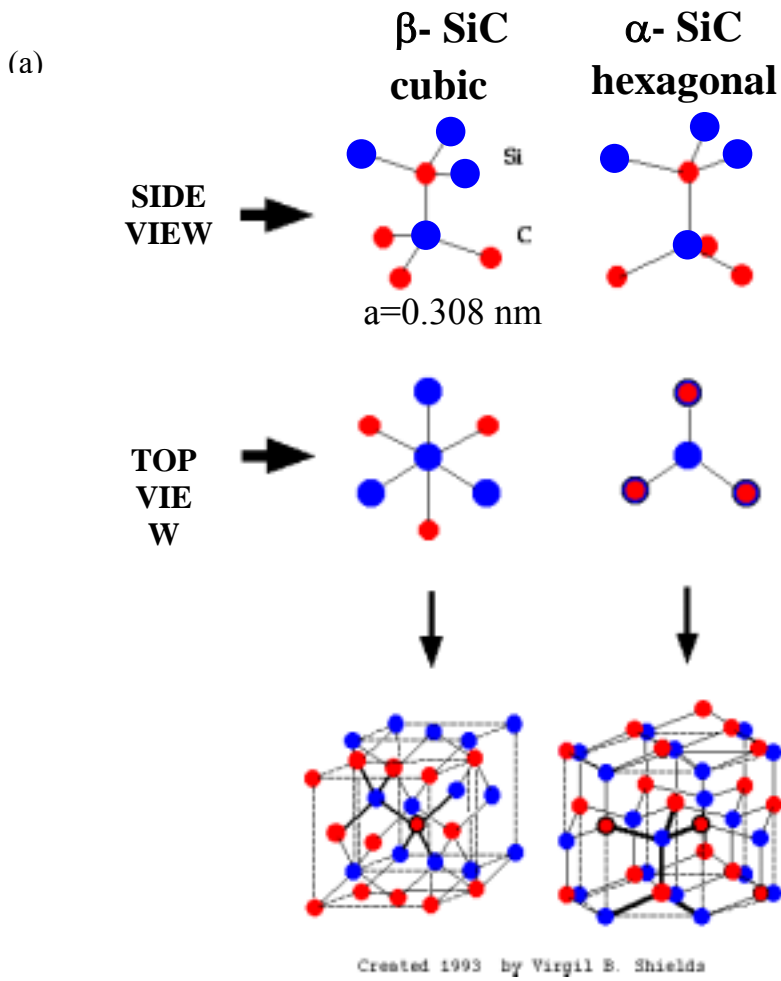


Figure 1-1: (a) Crystal structures and (b) stacking sequence for various SiC polytypes [16].

CHAPTER 2

AMBIENT TO HIGH-TEMPERATURE FRACTURE TOUGHNESS AND CYCLIC FATIGUE BEHAVIOR IN AL-CONTAINING SILICON CARBIDE CERAMICS

As mentioned in Chapter 1, this chapter will focus on experiments intended to explore the role of microstructure on the fracture and cyclic fatigue properties at ambient and at elevated temperatures. The material system chosen is a series of aluminum containing ABC-SiCs, whose microstructure, fracture and fatigue properties will be examined to understand the basic relationship between microstructure, toughening mechanisms, and fracture properties.

2.1 EXPERIMENTAL PROCEDURES

2.1.1 Materials Processing

Submicron β -SiC powder (Betarundum, Grade ultrafine, IBIDEN, Japan), with a mean particle size of 0.27 μm , was mixed with Al, B and C additives in toluene. The Al powder (H-3, Valimet, Stockton, CA), which had an average size of 3 μm , was added in amounts of 3, 5 and 7 wt.%, whereas the boron (Callery Chemical, Callery, PA) was kept constant at 0.6 wt.%. The carbon was introduced as 4 wt.% Apiezon wax, which on pyrolysis yielded ~ 2 wt.% C content. The slurry was ultrasonically agitated, stir-dried and sieved through a 200 mesh screen. After cold die compression at 35 MPa, the green compacts were hot-pressed at 1900°C for 1 h at 50 MPa pressure in graphite dies lined with graphite foil, under a constant gaseous argon flow at 7 kPa, to produce ~ 4 mm thick, 38 mm diameter disks. Unless noted, all results presented are from samples tested in the

as-processed state; however, for a few room temperature experiments specimens were tested after ~ 72 h at 1300°C in flowing argon, to see if prolonged exposure to elevated temperatures affects the room temperature properties.

2.1.2 Microstructure Characterization

After diamond grinding ~500 μm off each surface, both sides of the hot-pressed pellets were polished to a 1 μm finish. Densities of the hot-pressed specimens were determined by Archimedes' method and found to be greater than 99% of theoretical density for all samples.

X-ray diffraction (XRD) was carried out on the polished surfaces of the disks over the range from 20° to 80° (2θ) at steps of 0.05°, with a time constant of 1 s. Quantitative analysis of the SiC polytypes for each microstructure was carried out using the X-ray peak intensities by considering the four most common polytypes, 3C, 4H, 6H, and 15R, using the system of equations derived by Ruska *et al*; details of this method may be found in Ref. [1].

Grain morphology was observed using field-emission scanning electron microscopy (SEM) (secondary electron mode) of both polished and plasma etched specimens. High-resolution transmission electron microscopy (HRTEM) was performed to examine the nature of the grain boundaries using 3 mm diameter disks which were sliced from bulk SiC. After mechanical grinding and polishing down to 100 μm thick, the central area of each disk was dimpled to 10 μm thick, and then argon ion milled to make the samples electron transparent. Microstructural characterization was performed in a 200 kV field-emission-gun Philips CM200 transmission electron microscope, equipped with an energy-dispersive X-ray spectroscopy (EDS) system for chemical microanalysis.

2.1.3 Fracture and Fatigue Testing

2.1.3.1 *R-curve Test*

Resistance curves (R-curves) and fracture toughness K_c values were determined using fatigue precracked, 3 mm thick, disk-shaped compact-tension DC(T) samples (with a width of $W = 28$ mm), in general accordance with ASTM Standard E-399. The notch depth was ~ 9 mm ($\sim 0.3 W$), such that crack sizes, a , after precracking were typically 11 to 17 mm in length. Precracking was performed at ambient temperature by cyclic fatigue loading the DC(T) specimens, which contained half-chevron notches; procedures are described in ref. [2]. Prior to R-curve testing, precracked specimens were additionally cycled for ~ 24 hr at a stress-intensity range just below the ΔK_{th} fatigue threshold in an attempt to minimize the presence of bridging ligaments in the crack wake; no further crack extension was detected by compliance techniques or optical microscopy during this period. For 7ABC samples, fatigue precracking was not possible due to the inherent brittleness of this microstructure. Accordingly, to get an upper bound for the toughness, fracture toughness tests were conducted using “razor micronotched” samples with a root radius of ~ 20 μm instead of an atomically sharp precrack. Micronotches were produced by repeatedly rubbing a razor blade over the tip of a straight saw-cut notch in the presence of a 1 μm diamond slurry.

At ambient temperatures, R-curves were determined to evaluate the toughness of the 3ABC and 5ABC microstructures; however at elevated temperatures, due to the difficulty of conducting such tests at 1300°C, single-value fracture toughness values were obtained by computing K_c from the peak load at fracture using standard stress-intensity solutions [3]. Ambient-temperature tests were conducted in controlled room air (25°C, $\sim 45\%$

relative humidity), whereas all testing at higher temperatures was carried out in flowing argon gas at atmospheric pressure in an environmental chamber/furnace with graphite elements, which maintained the specified temperature to within $\pm 1^\circ\text{C}$.

2.1.3.2 Cyclic Fatigue Test at Room Temperature

Cyclic fatigue-crack growth testing was also performed at 25° and 1300°C in identical environments using similar-sized DC(T) specimens, in general accordance with ASTM Standard E-647, modified for brittle materials using procedures outlined in ref. [2]. Samples for testing at both low and high temperatures were initially fatigue precracked at ambient temperature, as described above. All testing was performed on computer-controlled MTS servo-hydraulic testing machines, operating at a test frequency of 25 Hz (sinusoidal waveform) and a tension-tension load ratio (ratio of minimum to maximum loads) of $R = 0.1$. Fatigue-crack growth rates, da/dN , were determined under stress-intensity K control over five decades of growth rates from threshold to instability ($\sim 10^{-11}$ to 10^{-6} m/cycle). The ΔK_{th} and $K_{\text{max,th}}$ fatigue thresholds, which were operationally defined at minimum growth rate of 10^{-10} – 10^{-11} m/cycle, were approached under decreasing K (load-shedding) conditions using a normalized K -gradient ($1/K \cdot dK/da$) of 0.1 mm^{-1} .

For both toughness and fatigue-crack growth tests, crack lengths were monitored at ambient temperatures using back-face strain, elastic unloading compliance methods [4]. Measurements were made with a 350Ω strain gauge (1.92 mm gauge length), affixed to the center of the back face of the test samples, using the numerical compliance relationship between crack length and back-face strain for the DC(T) specimen taken from ref. [5]. Crack lengths were continuously monitored *in situ* and recorded at 25 μm

increments; corresponding growth rates were computed by averaging over crack extensions of 100 μm .

2.1.3.3 *Cyclic Fatigue Crack Growth at High Temperature*

Corresponding crack length measurements at elevated temperatures were carried out using a direct-current electrical-potential drop method [6,7], which was made possible by the fact that there is a significant decrease in electrical resistivity ρ of silicon carbide above 600°C ($\rho \sim 10 \Omega\text{m}$). This approach involves passing a constant current through the DC(T) specimen and measuring the potential developed across the notch, using a relationship between voltage and crack length determined both numerically and experimentally in Ref. [5] for the DC(T) geometry. A constant direct current of ~400-800 mA was used so that the initial output potential was 0.4 V. Full details are given in refs. [6,7].

Due to crack bridging, errors were invariably incurred in the compliance and potential crack-length measurements; accordingly, verification of the crack length was achieved via optical microscopy. For elevated temperature tests, samples were periodically cooled down to ambient temperature to verify the crack size. Discrepancies between the compliance/electrical-potential and optically measured crack length were corrected by assuming that the error accumulated linearly with crack extension.

2.1.4 **Fractography**

Fracture surfaces and corresponding crack paths for cracks grown under both monotonic and cyclic loads were examined in the SEM in the secondary electron mode. The crack paths were used to examine how the crack interacted with the salient features of the microstructure, and were obtained by metallographically polishing sections taken

perpendicular to the crack surface. Additionally, the damage regions around the crack tip after fatigue cycling were examined using TEM, with specimens prepared as described above, using special care to ensure that the crack tips were in the thinnest, electron transparent, region.

2.1.5 Crack-Opening Profile Measurements

To assess the differences in grain bridging, crack-opening profile measurements were made by *in situ* loading one 3ABC and one 5ABC sample with almost identical crack lengths in the field-emission SEM, after R-curve measurements had been made. Each sample was loaded to an applied driving force of $6.2 \text{ MPa}\sqrt{\text{m}}$, corresponding to ~90% of the driving force need for crack extension in the 3ABC material (i.e., peak toughness). Measurements of the full crack opening, $2u$, were made at a resolution of 10 nm at magnifications of up to 30,000X near the crack tip. The crack lengths were also measured *in situ* to be sure crack extension did not occur during loading. Readings were made at ~50 μm increments to give an adequate number of data points to get a reasonable estimate of the average crack-opening behavior.

2.2 RESULTS

2.2.1 Microstructure Features

2.2.1.1 Phase and Grain Morphology

Three quite distinct microstructures were obtained after hot pressing ABC-SiC with the different Al contents of nominally 3, 5 and 7 wt.% (Fig. 2.1). In 3ABC-SiC, elongated grains corresponding to the hexagonal 4H or 6H α -SiC phases were most prevalent (Fig. 2.1a). Their size and shape were relatively uniform, with lengths and

widths of, respectively, $l \sim 4$ to $7 \mu\text{m}$ and $w \sim 1\text{-}2 \mu\text{m}$, and an aspect ratio of ~ 5 . Submicron, equiaxed SiC grains corresponding to cubic 3C β -SiC phase were also observed.

Increasing nominal Al content to 5 wt.% caused marked microstructural changes, with a bimodal structure being formed comprising a significant volume fraction of both elongated and equiaxed SiC grains (Fig. 2.1b). The higher Al additions in 5ABC-SiC apparently promoted anisotropic growth of the elongated grains, resulting in an aspect ratio of ~ 23 , almost five times that of 3ABC-SiC.

This trend was continued with additional increases in Al content. In 7ABC-SiC, the aspect ratio of the elongated α -SiC grains was further increased to ~ 32 ; however, the proportion of such grains was significantly reduced with the submicron equiaxed β -SiC grains becoming predominant (Fig. 2.1c). Detailed microstructural characteristics for the three microstructures from Ref. [8] are summarized in Table 2.1.

2.2.1.2 Grain Boundaries

In addition to the differing phase and grain morphology, the other major distinction in the three microstructures was in the nature of the grain boundaries. During the liquid-phase sintering, nanoscale intergranular films are typically formed between SiC grains. As reported previously [9], TEM studies revealed that the intergranular films in as-processed 3ABC-SiC were amorphous (Fig. 2.2) with an Al-rich composition, as determined by EDS analysis. With increasing Al content, segregation of the Al atoms to the intergranular films was found to be increased by 32% and appeared to be saturated and constant for both 5ABC and 7ABC, although considerable amounts of free Al were detected in the latter structure.

With respect to the structure of the boundaries, whereas the intergranular films were fully amorphous in 3ABC and fully crystalline in 7ABC, both amorphous and crystalline films were frequently observed in 5ABC (Fig. 2.2). It should be noted that epitaxial crystalline grain-boundary films were often formed on the (0001) grain-boundary surface of the matrix α -SiC grains. This epitaxial growth is attributed to the fact that one of the identified phases for the crystalline films was 2H-wurtzite, which is similar in structure to the 4H- or 6H-SiC matrix grains [9]. Because of this epitaxial growth, crystalline grain-boundary films are not always easily seen in high-resolution TEM images like the ones shown in Fig. 2.2; however, the consistent detection of two to three monolayers of Al segregation in the boundaries was reliably used to confirm the existence of these films.

Table 2.1. Comparison of Microstructures of ABC-SiC (after Ref. [8])

| | | 3ABC-SiC | 5ABC-SiC | 7ABC-SiC |
|--|---------------------|---|---|--|
| Grain Structures | | Uniform long | Bimodal | Equiaxed* |
| Grain Size (μm) & Aspect Ratio | Elongated Grains | $l = 4.4 \pm 1.4$ $w = 1.0 \pm 0.3$ $l/w = 4.7 \pm 0.6$ | $l = 20 \pm 6.4$ $w = 0.8 \pm 0.3$ $l/w = 23.2 \pm 6.8$ | $l = 11.5 \pm 5.8$ $w = 0.4 \pm 0.2$ $l/w = 31.6 \pm 15.4$ |
| | Equiaxed | | 0.6 ± 0.2 | 0.6 ± 0.3 |
| Area Density of Elongated Grains (mm^{-2}) | | 85,000 | 45,000 | 23,000 |
| Phase & Volume Fraction | | 70% 4H 30% 3C | 12% 4H, 21% 6H 67% 3C | 20% 6H 80% 3C |
| Grain Boundaries | | Amorphous | Partially crystallized | Fully crystallized |

*With a few needle-like elongated grains

The microstructures of the samples subjected to 72 hr exposures at 1300°C were essentially identical to those of as-hot-pressed conditions, except that the grain boundaries were all crystallized in 3, 5 and 7ABC.

2.2.2 Fracture Toughness and Strength

2.2.2.1 Fracture Toughness

The variation in fracture toughness at 25° and 1300°C with Al wt.% is summarized in Table 2.2. For both as-hot-pressed and annealed 3ABC and 5ABC structures at 25°C, R-curves were determined and are shown in Fig. 2.3. Peak values from the R-curves indicate that in as-hot-pressed condition, 5ABC is some 17% tougher than 3ABC; both these structures are essentially twice as tough as 7ABC, which displayed a fracture toughness K_c value no greater than 4.0 MPa \sqrt{m} , comparable to that of commercial SiC (e.g., Hexaloy SA). Results for 3ABC and 5ABC at elevated temperatures showed a reduction in the fracture toughness at 1300°C of roughly 20 to 40%, while 7ABC had an ~20% increase. Finally, experiments using samples pre-exposed for 72 hr at 1300°C prior to room temperature testing showed that although grain-boundary crystallization occurred, there was no significant effect on the toughness (Table 2.2); the toughness of 3ABC and 5ABC showed a 16% increase and 26% decrease, respectively.

Table 2.2. Comparison of Mechanical Properties of ABC-SiC

| | 3ABC-SiC | 5ABC-SiC | 7ABC-SiC |
|--|----------|----------|-----------------------|
| Strength at 25°C, (Ref. [8]) 4-pt bending (MPa) | 691 ± 12 | 480 ± 30 | 533 ± 58 |
| Toughness K_c at 25°C (MPa \sqrt{m}) | 7.6 | 8.9 | 4.0* (upper bound) |
| Toughness K_c at 1300°C (MPa \sqrt{m}) | 4.5 | 7.4 | 4.9* (upper bound) |
| Toughness K_c of pre-exposed samples at 25°C (MPa \sqrt{m}) | 8.8 | 6.6 | — |

*Toughness evaluated from a razor micro-notch.

2.2.2.2 Strength

For comparison, ambient temperature four-point bend strength results from Ref. [8] for all three of the as-hot-pressed ABC-SiCs are given in Table 2.2 where each value represents the average of five measurements along with the standard deviation. All three microstructures displayed strengths near or in excess of ~500 MPa. 3ABC had a 30 to 40% higher bend strength than either the 5ABC and 7ABC structures, which showed comparable strength levels.

2.2.3 Fatigue-Crack Growth Behavior

The variation in fatigue-crack growth rates, da/dN , with applied stress-intensity range, ΔK , for 3ABC- 5ABC- and 7ABC-SiC at 25° and 1300°C is shown in Fig. 2.4. The da/dN vs. ΔK data were fit to a simple Paris power-law formulation:

$$da/dN = C'\Delta K^m, \quad (2.1)$$

where C' and m are scaling constants. Values of these constants, together with a summary of the fatigue threshold data, are listed in Table 2.3. All curves show very high Paris-law exponents ($m > 40$), which are typical of brittle materials, and have $K_{\max,th}$ thresholds that approach 80~90% of the fracture toughness, K_c (with the exception of 7ABC). It should be noted that the Paris-law exponent for 5ABC is about twice that for 3ABC, which suggests a difference in fatigue mechanism (as discussed below).

It is apparent that fatigue-crack growth resistance scales with the fracture toughness in SiC. Considering first the ambient-temperature results, the 5ABC structure, with a $K_{\max,th}$ threshold of 7.9 MPa \sqrt{m} , displayed the best properties followed by 3ABC, where $K_{\max,th} \sim 5.9$ MPa \sqrt{m} . The 7ABC structure was so brittle that it simply failed catastrophically when the ambient temperature fracture toughness was reached, i.e., when $K_{\max} = K_c \sim 3 - 4$ MPa \sqrt{m} ; this structure showed no susceptibility to fatigue failure. With increasing

temperature from 25° to 1300°C, fatigue thresholds were reduced for 3ABC and 5ABC, reflecting the lower toughnesses at high temperature; however, the Paris-law exponents were very similar to their room temperature values, which is indicative of similar damage mechanisms being active at low and high temperatures.

Table 2.3. Cyclic fatigue-crack growth properties for ABC-SiC tested at $R=0.1$, $\nu=25\text{Hz}$

| | Testing Temperature (°C) | Fatigue Thresholds | | Critical Toughness, K_c (MPa $\sqrt{\text{m}}$) | $K_{\text{max,th}}/K_c$ | Paris Law $da/dN=C'\Delta K^m$ | |
|------|--------------------------|---|--|--|-------------------------|--------------------------------|------------------------|
| | | ΔK_{th} (MPa $\sqrt{\text{m}}$) | $K_{\text{max,th}}$ (MPa $\sqrt{\text{m}}$) | | | M | C' |
| 3ABC | 25° | 5.3 | 5.9 | 7.6 | 0.78 | 45 | 4.4×10^{-41} |
| | 1300° | 3.5 | 3.9 | 4.5 | 0.87 | 44 | 4.3×10^{-34} |
| 5ABC | 25° | 7.1 | 7.9 | 8.9 | 0.88 | 133 | 9.5×10^{-124} |
| | 1300° | 6.1 | 6.8 | 7.4 | 0.92 | 107 | 3.7×10^{-95} |

2.2.4 Fractography and Crack Paths

Overload fracture surfaces from the fracture toughness samples show a transition of increasing transgranular fracture with increasing Al content from 3 to 7 wt.% (Fig. 2.5); however, even for 7ABC there is still some intergranular fracture between the fine grains. SEM micrographs of the crack-path trajectories in Fig. 2.6a confirms the intergranular fracture mode in 3ABC, and provides evidence that crack-tip shielding by individual grain bridging (frictional bridging) in the crack wake is the primary toughening mechanism in this structure, as reported in refs. [6,10-13]. This mechanism of grain bridging pertains to behavior in 3ABC at both the low and high temperatures (Fig. 2.6b). Crack bridging is also apparent in the 5ABC structure at both 25° and 1300°C; however, the primary mechanism is quite different (Fig. 2.6c-f). Here, the majority of bridges are composed of uncracked ligaments of SiC which span the crack wake. Uncracked-ligament bridging is a toughening mechanism observed in many materials, including

metal-matrix composites [14], γ -based TiAl intermetallics [15], and even human bone [16]. Such ligaments were typically composed of one or more elongated grains; indeed, the crack path in both the 3ABC and 5ABC microstructures appeared to preferentially seek out these α -SiC grains. In contrast, the crack path in the as-processed 7ABC microstructure is predominantly transgranular through both the equiaxed and elongated grains, with no evidence of any form of bridging.

Corresponding fatigue fracture surfaces for the 3ABC and 5ABC structures were essentially identical to the overload fracture surfaces, except for the presence of debris. Such observations are consistent with the generally accepted mechanisms for the fatigue of grain-bridging ceramics, involving (i) damage (crack-advance) mechanisms ahead of the crack tip essentially identical to those under monotonic (non-cyclic) loading, and (ii) the progressive degradation of grain bridging with cyclic loading behind the crack tip, associated with such processes as frictional wear in the sliding grain boundaries and the cracking/crushing of crack-surface asperities [10,17,18].

As noted above, fracture surfaces and crack paths at 1300°C are of similar nature to that at room temperatures, with clear evidence of grain bridging and no evidence of creep damage in the form of softening of the intergranular films and resulting grain-boundary cavitation. This is apparent from high magnification TEM images of the crack-tip regions in 3ABC and 5ABC after fatigue-crack growth at high temperatures (Fig. 2.7). Indeed, based on the fractographic characterization and the results presented in Figs. 2.6 and 2.7, we can conclude that the mechanisms of fracture and fatigue-crack propagation in both these microstructures are essentially unchanged between 25° and 1300°C.

2.2.5 Crack-Opening Profile Results

Clearly, both toughening and fatigue-crack growth in the 3ABC and 5ABC structures are markedly influenced by the presence of crack bridging. In order to verify the existence of such crack-tip shielding, crack-opening profiles were measured for two cracks in samples used for R-curve testing, which were then loaded *in situ* in the field-emission SEM to a stress intensity of $6.2 \text{ MPa}\sqrt{\text{m}}$; results are shown in Fig. 2.8 and are compared with the computed crack-opening profile for an elastic traction-free crack at the same applied K . In this figure, it can be seen that measured crack openings are significantly smaller than that expected for a traction-free crack, clearly implying the presence of crack bridging in both samples. Furthermore, the crack in the 5ABC-SiC sample has a smaller opening than that for the 3ABC-SiC sample, indicative of more potent bridging in the 5ABC microstructure.

These differences in the degree of crack bridging can be quantified by fitting the near-tip crack-opening profile to the Irwin crack-opening displacement solution for a linear elastic crack in order to obtain the near-tip stress intensity, K_{tip} (Appendix 2.1):

$$u_{\text{tot}}(x) = \frac{K_{\text{tip}}}{E'} \sqrt{\frac{8(a-x)}{\pi}} \quad , \quad (2.2)$$

where E' is Young's modulus (E in plane stress, $E/(1-\nu^2)$ in plane strain, where ν is Poisson's ratio), and x is the position of interest with origin at the load line. Regressions of the crack-tip opening profile data for the first $70 \mu\text{m}$ after the crack tip yield a value of $2.5 \text{ MPa}\sqrt{\text{m}}$ for 3ABC and $1.6 \text{ MPa}\sqrt{\text{m}}$ for 5ABC. Accordingly, considering that K_{tip} may be expressed as:

$$K_{\text{tip}} = K_{\text{app}} - K_{\text{br}} \quad , \quad (2.3)$$

where K_{app} is the applied stress intensity (6.2 MPa \sqrt{m}) and K_{br} is the contribution due to bridging, K_{br} is determined to be 3.7 MPa \sqrt{m} for 3ABC and 4.6 MPa \sqrt{m} for 5ABC. It should be noted that, at the same applied stress intensity, the 5ABC microstructure develops the higher contribution from bridging, and the lower driving force experienced at the crack tip.

2.3 DISCUSSION

2.3.1 Toughening Mechanisms

Characterization of the observed crack paths (Fig. 2.6) along with the crack opening profile measurements (Fig. 2.8) affirm that crack bridging is the primary toughening mechanism in 3ABC and 5ABC-SiC; in contrast, no bridging was observed in the as-processed 7ABC microstructure which had the lowest fracture toughness, comparable to that of commercial silicon carbides. For 3ABC-SiC, frictional bridging appears to be dominant whereby bridging stresses are developed by the frictional resistance to pullout and mechanical interlocking of grains which interact across the crack wake, schematically shown in Fig. 2.9a. Such frictional grain bridging is a common toughening mechanism for a variety of ceramic materials which fracture intergranularly [10,19-22].

Conversely, observations of cracking in the 5ABC microstructure indicate a change in toughening mechanism to uncracked-ligament, or elastic, bridging; with this change in mechanism there is an associated increase in toughness. As seen in Fig. 2.6c,d,e, uncracked ligaments, often several grains in size, were observed to bridge the crack wake in the 5ABC microstructure; frictional bridges, such as those seen in 3ABC (Fig 6a,b), were far less common. Such ligaments apparently form as a result of local crack arrest at

microstructural inhomogeneities, which leaves unfractured ligaments in the crack wake, due to either non-uniform advance of the crack front or crack nucleation ahead of the main crack tip; this phenomenon is illustrated in Fig 9b. However, it is currently unclear what causes the transition from predominantly frictional to uncracked-ligament bridging, although this change must be related to the notable differences in microstructure and to the grain-boundary film properties. Specifically, the dominant local arresting points responsible for the formation of such uncracked ligaments may be attributed to large elongated grains oriented favorable for local crack deflection, as illustrated in Fig. 2.9b, and/or to spatial variations in grain boundary strengths due to structure¹ or chemistry differences. Since the crack path follows the elongated grains almost exclusively, the higher aspect ratio and smaller fraction of elongated grains in the 5ABC, as compared to the 3ABC, structure undoubtedly promotes larger off-angle deflections as the crack propagates along the boundary of the α -SiC grains; thus, with the next α grain further away than in the 3ABC SiC, uncracked ligaments are more probable, as shown schematically in Fig. 2.9b. Uncracked-ligament bridges are expected to be more potent than frictional bridges in that they should be able to sustain higher loads before failing. This is consistent with the higher toughness and the higher deduced bridging stress intensity, K_{br} , of the 5ABC structure (described above), both of which confirm the enhanced degree of bridging where uncracked ligaments predominate.

Finally, the behavior of 7ABC is illustrated in Fig. 2.9c. Here, unlike the 3ABC and 5ABC microstructures, the crack path is predominantly transgranular, and proceeds through both the equiaxed β - and elongated α -SiC grains, with very few cases of

¹ While amorphous and the 2H-wurtzite crystalline phase has been positively identified for some boundaries, other boundary structures may also exist.

intergranular fracture. With such a cracking morphology, there was no evidence of any form of bridging.

The fracture toughness values for both 3ABC- and 5ABC-SiC are slightly lower at 1300°C than their corresponding room temperature values, which is in agreement with previous results on 3ABC-SiC [6]. Such a drop in toughness may be related to changes in the residual stress state, either by the relaxation of thermal mismatch stresses which, along with mechanical interlocking, may contribute to the tractions acting on the frictional bridges [20,23,24], or by altering the mismatch stresses in triple point junctions, which has been shown to affect the toughness of silicon nitride [25]. It should be noted that 3ABC-SiC, which has a larger proportion of frictional bridges, experiences a larger drop in toughness compared to 5ABC-SiC. Such a result is consistent with a reduction in thermal stresses affecting the frictional bridging tractions, suggesting that the former mechanism indeed plays a role here.

While exposure to 1300°C is known to affect the microstructure of ABC-SiCs, by the crystallization of amorphous grain boundaries, along with associated chemistry changes, and the formation of nano-precipitates within the SiC grains [9,26], only minor effects on the subsequent low-temperature toughness were evident. Thus, it may be concluded that although the crystalline boundaries have a very positive impact on the high-temperature creep resistance of 3ABC and 5ABC silicon carbides [27], either amorphous or crystalline boundaries are sufficiently brittle to give intergranular fracture and hence high toughness in these materials at lower temperatures (see also ref. [13]).

Finally, it should be noted that although the 5ABC microstructure has the highest toughness, it also has the lowest strength (Table 2.2). This inverse dependence of strength

and toughness may be attributed to the fact that 5ABC-SiC has a larger (elongated) grain size, and correspondingly is expected to have larger initial flaw sizes. Although 7ABC-SiC has the lowest toughness, its strength is comparable to that of 5ABC-SiC, again from smaller initial flaw sizes due to the smaller grains. The 3ABC microstructure achieves its relatively high fracture toughness with the smallest grain size, and accordingly, has the highest strength of the three microstructures.

2.3.2 Cyclic Fatigue Mechanisms

Since the fatigue of brittle materials such as SiC is invariably controlled by the progressive degradation under cyclic loading of the prevalent extrinsic toughening (crack-tip shielding) mechanisms, a sound strategy for improving resistance to fatigue-crack growth is by making the shielding mechanisms more resilient in the presence of such cyclic loads. In this regard, in addition to providing increased toughening, uncracked-ligament bridges are significantly less susceptible to fatigue damage during cyclic loading since the cycle-dependent interfacial wear mechanisms that occur to degrade frictional bridges [18] are not relevant. Instead of wear of the sliding boundaries, the degradation of the uncracked-ligament bridges must occur by a fracture process, presumably when a critical failure stress is reached, a mechanism that is likely to be cycle-independent. Indeed, a reduced susceptibility to cyclic fatigue was observed in 5ABC-SiC, which is toughened primarily by such ligament bridging, as reflected by the much higher Paris-law exponents (i.e., steeper $da/dN-\Delta K$ curves) (Table 2.3). This was especially apparent at 1300°C where fatigue data was unattainable for the 5ABC microstructure over much of the range of crack-growth rates due to unstable fracture of the specimens.

Thus, by increasing the Al content in ABC-SiC to ~5 wt.%, which leads to a microstructure of high aspect-ratio α -SiC grains with both amorphous and crystalline grain-boundary films, which in turn causes a change in the predominant crack-tip shielding mechanism from frictional to uncracked-ligament bridging, optimal crack-growth resistance at 25° and 1300°C can be obtained under both monotonic and cyclic loading. Not only is the ligament bridging mechanism a more potent mode of toughening in ABC silicon carbides, but it also is more resistant to degradation under cyclic loading and thus leads to a reduced susceptibility to fatigue failure.

2.4 CONCLUSIONS

An experimental study has been made of the microstructural and mechanistic origins of the fracture toughness and fatigue-crack growth resistance of a series of Al-containing ABC-silicon carbides at 25° and 1300°C, the following conclusions can be made:

- (1) Of the three silicon carbides examined here (3, 5, and 7ABC SiC), 5ABC-SiC demonstrated the highest peak toughness of 8.9 MPa \sqrt{m} at 25°C and 7.1 MPa \sqrt{m} at 1300°C. These high toughness values were attributed to crack-tip shielding, primarily from *uncracked-ligament* bridging in the crack wake. Corresponding toughening in 3ABC-SiC was primarily associated with *frictional* grain bridging; this structure displayed roughly 15% lower toughness. No bridging was detected in 7ABC microstructure, which accordingly exhibited the lowest toughness, comparable to that of commercial SiC.

- (2) Whereas the 7ABC structure was too brittle to be susceptible to fatigue, 3ABC and 5ABC exhibited cyclic fatigue-crack growth at stress intensities above a $K_{\max,th}$ threshold which was roughly 80 – 90% of the peak toughness.
- (3) Fatigue-crack growth in 3ABC and 5ABC was associated the suppression of crack bridging in the crack wake. In general, the 5ABC microstructure was less susceptible to fatigue, as evidenced by its steeper $da/dN-\Delta K$ curve. This was attributed to the higher resilience of uncracked-ligament bridging to degradation under cyclic loading, as compared to frictional grain bridging in 3ABC.
- (4) While both the fracture toughness values and fatigue thresholds for 3 and 5ABC-SiC were found to be lower at 1300°C, the mechanisms of toughening and fatigue-crack propagation were found to be the same as at 25°C. No evidence of creep cavitation damage was detected during the fatigue testing at 1300°C.

APPENDIX 2.1

THE VALIDITY OF ESTIMATING $K_{I,TIP}$ BY IRWIN NEAR TIP SOLUTION

The crack opening displacements u_{tot} can be viewed as the superposition of the bridging-free crack opening u_{app} and the suppressed crack opening u_{br} due to the bridging stress σ_{br} [28]:

$$u_{tot}(x) = u_{app}(x) - u_{br}(x) \quad (A2.1)$$

These displacements, in LEFM, are related to the stress intensity factors and their loading sources by the weight function (which will be discussed in Appendix 3.1) as stated below:

$$u_{app}(x) = \frac{1}{E'} \int_x^a K_{app}(a') h(a', x) da' \quad (A2.2)$$

$$u_{br}(x) = \frac{1}{E'} \int_0^a \int_{\max(x, x')}^a h(a', x) h(a', x') \sigma_{br}(x') da' dx' \quad (A2.3)$$

where E' is Young's modulus (E in plane stress, $E/(1-\nu^2)$ in plane strain, where ν is Poisson's ratio), and x is the position of interest with origin at the load line. The geometry specific weight function, h , for the DC(T) specimen may be expressed as [28]:

$$h(a, x) = \sqrt{\frac{2}{\pi a}} \frac{1}{\sqrt{1-x/a}} \left[1 + \sum_{(\nu, \mu)} \frac{A_{\nu\mu} (a/W)^\mu}{(1-a/W)^{3/2}} (1-x/a)^{\nu+1} \right] \quad (A2.4)$$

where the coefficients $A_{\nu\mu}$ may be found in ref. [28]. Changing the integral sequence of x' and a' in the second term in (A2.3), we can rewrite it as

$$\begin{aligned} u_{tot}(x) &= \frac{1}{E'} \int_x^a K_{app}(a') h(a', x) da' - \frac{1}{E'} \int_0^a \int_{\max(x, x')}^a h(a', x) h(a', x') \sigma_{br}(x') da' dx' \\ &= \frac{1}{E'} \int_x^a K_{app}(a') h(a', x) da' - \frac{1}{E'} \int_x^a h(a', x) \left(\int_0^{a'} h(a', x') \sigma_{br}(x') dx' \right) da' \\ &= \frac{1}{E'} \int_x^a K_{app}(a') h(a', x) da' - \frac{1}{E'} \int_x^a K_{br}(a') h(a', x) da' \\ &= \frac{1}{E'} \int_x^a K_{tip}(a') h(a', x) da' \end{aligned} \quad (A2.5)$$

where $K_{tip} = K_{app} - K_{br}$. Suppose the crack tip stress intensity, K_{tip} , is continuous along the crack, then K_{tip} can be viewed as constant near the crack tip ($x \rightarrow a$), and equation (A2.5) is reduced to:

$$u_{tot}(x) = \frac{K_{tip}}{E'} \int_x^a h(a', x) da' \quad (A2.6)$$

As geometric effects in weight function can be ignored at the crack tip, equation (A.2.6) is simplified to the familiar Irwin COD solution, which is only applicable to an infinite large plate where boundaries don't affect the crack opening displacements:

$$u_{tot}(x) = \frac{K_{tip}}{E'} \sqrt{\frac{8(a-x)}{\pi}} \quad (A2.7)$$

In this case, the CODs considered are only within 70 μm to the crack tip, and the influence of the boundaries can be ignored; consequently, the Irwin equation (A.2.7) is valid for this near-tip solution.

REFERENCES

- [1] Ruska J, Gauckler LJ, Lorenz JL, Rexer HU. *Journal of Materials Science* 1979;14:2013.
- [2] Dauskardt RH, Ritchie RO. *Closed Loop* 1991;17:7.
- [3] Murakami Y. *Stress Intensity Factors Handbook*. Pergamon Press, 1987. p. 640.
- [4] Ritchie RO, Yu W. *Small Fatigue Cracks*. Lankford J, Lankford JLankford Js. TMS-AIME, Warrendale, PA,1986, 167.
- [5] Gilbert CJ, McNaney JM, Dauskardt RH, Ritchie RO. *Journal of Testing and Evaluation* 1994;22:117.
- [6] Chen D, Gilbert CJ, Zhang XF, Ritchie RO. *Acta Materialia* 2000;48:659.
- [7] Chen D, Gilbert CJ, Ritchie RO. *Journal of Testing and Evaluation* 2000;28:236.
- [8] Zhang XF, Yang Q, De Jonghe LC. *Acta Materialia* 2003;51:3849.
- [9] Zhang XF, Sixta M, De Jonghe LC. *Journal of the American Ceramic Society* 2000;83:2813.
- [10] Gilbert CJ, Cao JJ, MoberlyChan WJ, De Jonghe LC, Ritchie RO. *Acta Metallurgica et Materialia* 1996;44:3199.
- [11] Gilbert CJ, Ritchie RO. *Acta Materialia* 1998;46:609.
- [12] Chen D, Sixta ME, Zhang XF, De Jonghe LC, Ritchie RO. 2000, 4599.
- [13] Chen D, Zhang XF, Ritchie RO. *Journal of the American Ceramic Society* 2000;83:2079.
- [14] Shang JK, Ritchie RO. *Metallurgical Transactions* 1989;20A:897.
- [15] Chan KS. *Metallurgical Transactions* 1993;24A:569.
- [16] Nalla RK, Kinney JH, Ritchie RO. *Nature Materials* 2003;2:164.
- [17] Gilbert CJ, Dauskardt RH, Ritchie RO. *Journal of the American Ceramic Society* 1995;78:2291.
- [18] Lathabai S, Rödel J, Lawn B. *Journal of the American Ceramic Society* 1991;74:1348.
- [19] Swanson PL, Fairbanks CJ, Lawn BR, Mai Y-W, Hockey BJ. *Journal of the American Ceramic Society* 1987;70:279.
- [20] Bennison SJ, Lawn BR. *Acta Metallurgica* 1989;37:2659.
- [21] Mai Y-W, Lawn BR. *Journal of the American Ceramic Society* 1987;70:289.
- [22] Li C-W, Lee D-J, Lui S-C. *Journal of the American Ceramic Society* 1992;75:1777.
- [23] Swain MV. *Journal of Materials Science Letters* 1986;5:1313.
- [24] Kokaly MT, Tran DK, Kobayashi AS, Dai X, Patel K, White KW. *Materials Science & Engineering* 2000;A285:151.
- [25] Pezzotti G, Kleebe H-J. *Journal of the European Ceramic Society* 1999;19:451.
- [26] Zhang XF, Sixta ME, Chen D, De Jonghe LC. *Journal of Materials Science* 2001;36:5447.
- [27] Sixta M, Zhang XF, De Jonghe LC. *Journal of the American Ceramic Society* 2001;84:2022.
- [28] Fett T, Munz D. *Stress Intensity Factors and Weight Functions*. Computational Mechanics Publications, 1997. p. 408.

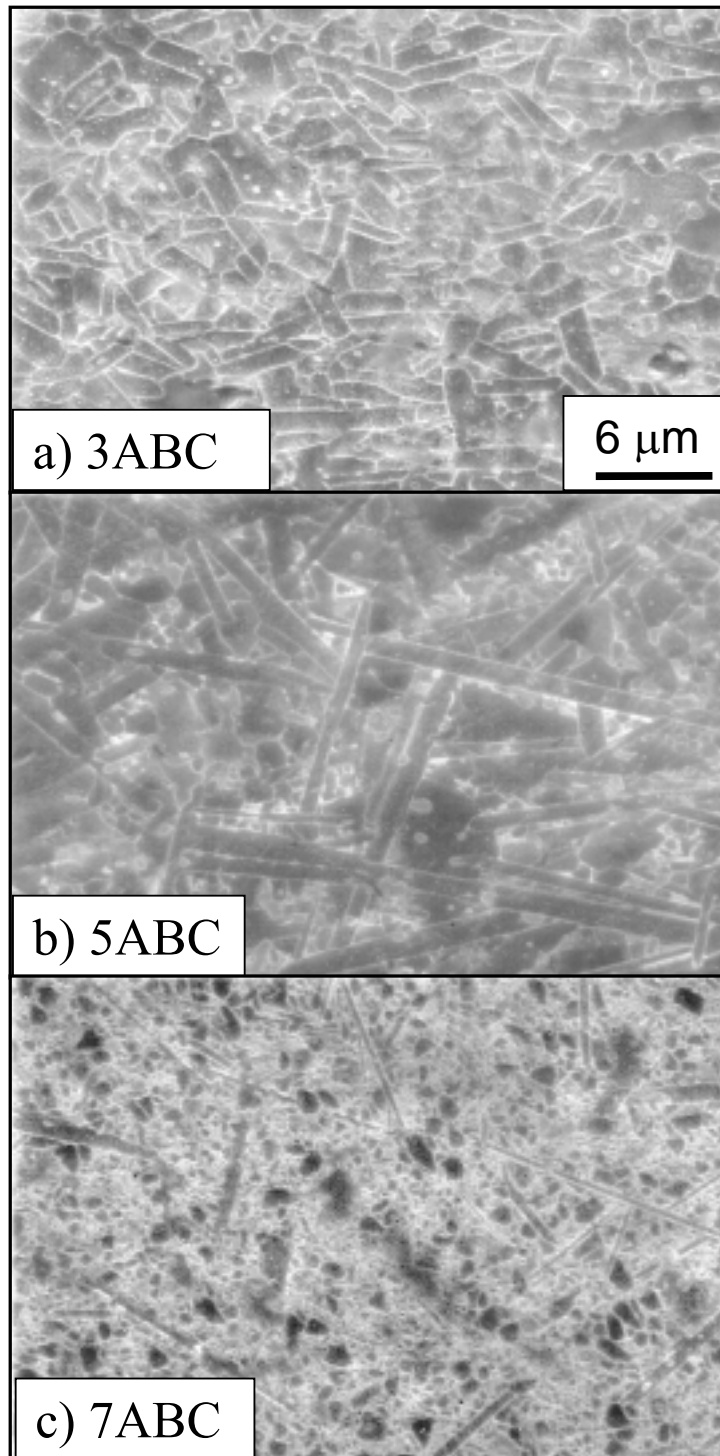


Fig. 2.1. SEM micrographs of etched surfaces of ABC-silicon carbides, showing the characteristic grain structures: (a) uniformly elongated grains in 3ABC, (b) bimodal structure of elongated (α -SiC) and equiaxed (β -SiC) in 5ABC, and (c) equiaxed grains with sparsely distributed needle-like grains in 7ABC. (Courtesy of Qing Yang)

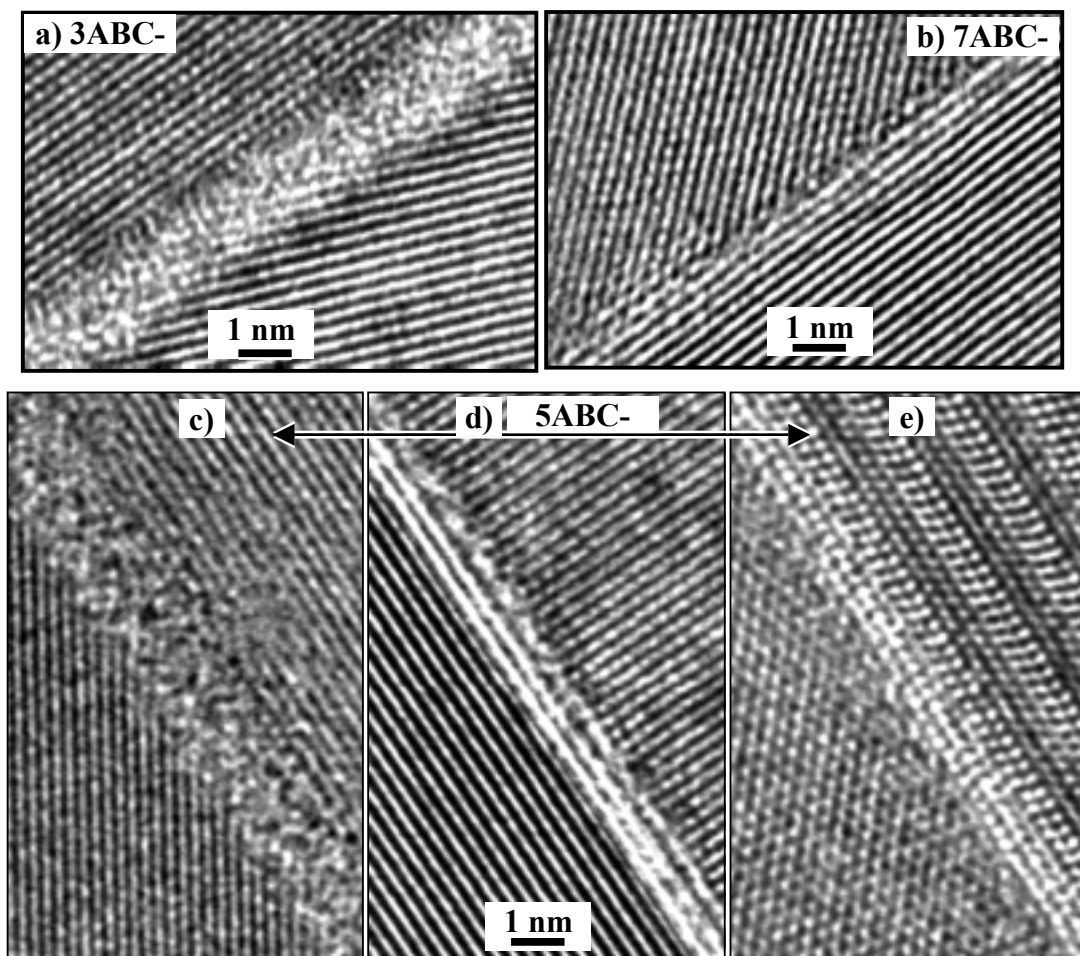


Fig. 2.2. High-resolution TEM micrographs showing the nature of the grain-boundary films in hot-pressed SiC with different Al content, showing (a) amorphous films in 3ABC, (b) fully crystallized films in 7ABC, and (c) amorphous, (d) partially crystallized and (e) fully crystallized films in 5ABC. (Courtesy of Dr. Xiao-Feng Zhang)

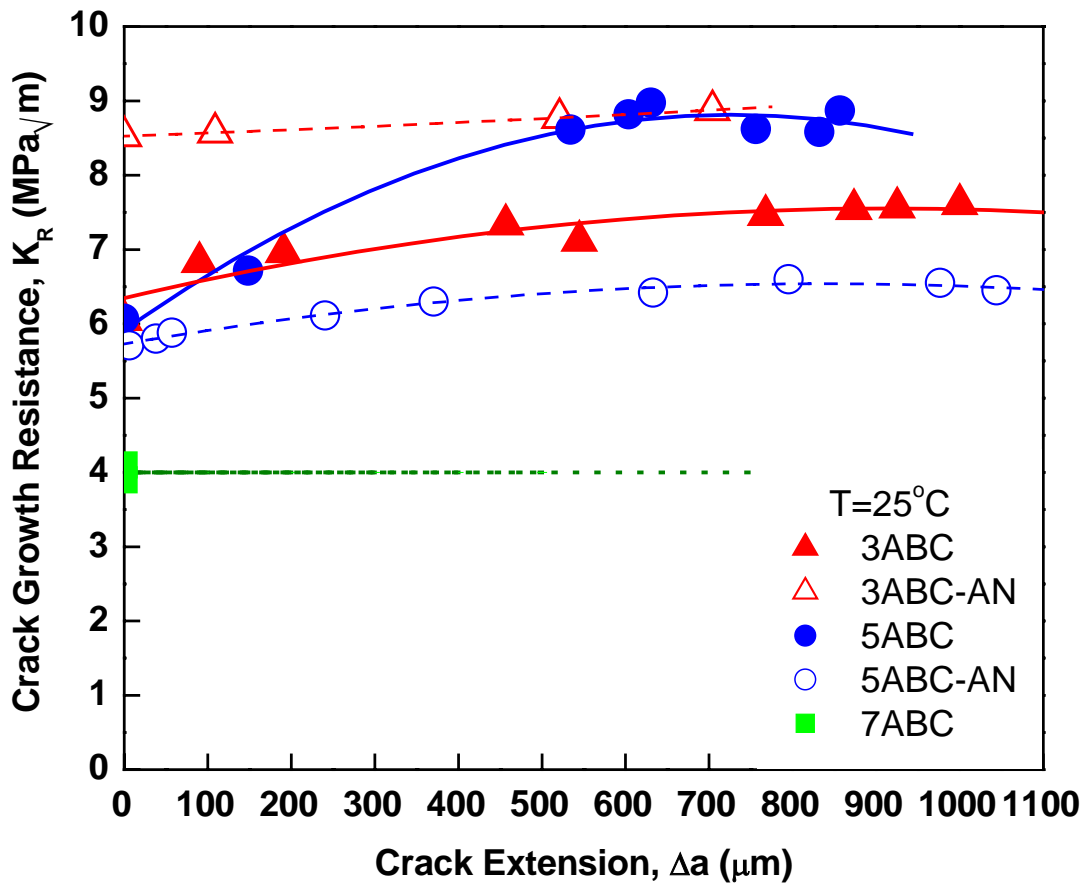


Fig. 2.3. Crack growth resistance, K_R , plotted as a function of crack extension, Δa , for as-hot-pressed and annealed xABC-SiC at room temperature.

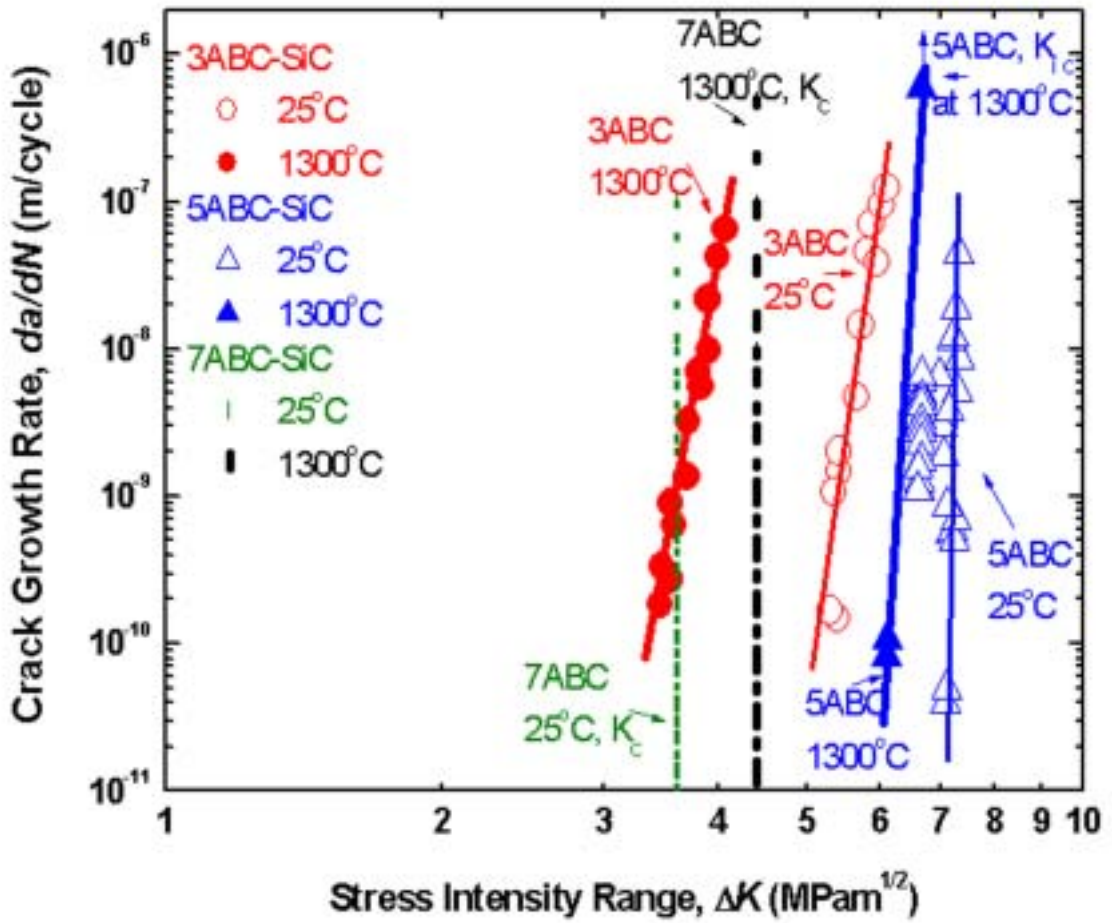


Fig. 2.4. Cyclic fatigue-crack growth rates, da/dN , at $R = 0.1$ in ABC-SiC, as a function of the applied stress-intensity range, ΔK , at temperatures of 25° and 1300°C. Note that 7ABC is sufficiently brittle that it exhibits no subcritical crack growth, i.e., it fails catastrophically once $K_{max} > K_c$; the dashed curve for this structure is drawn where $K_{th,max} = K_c$.

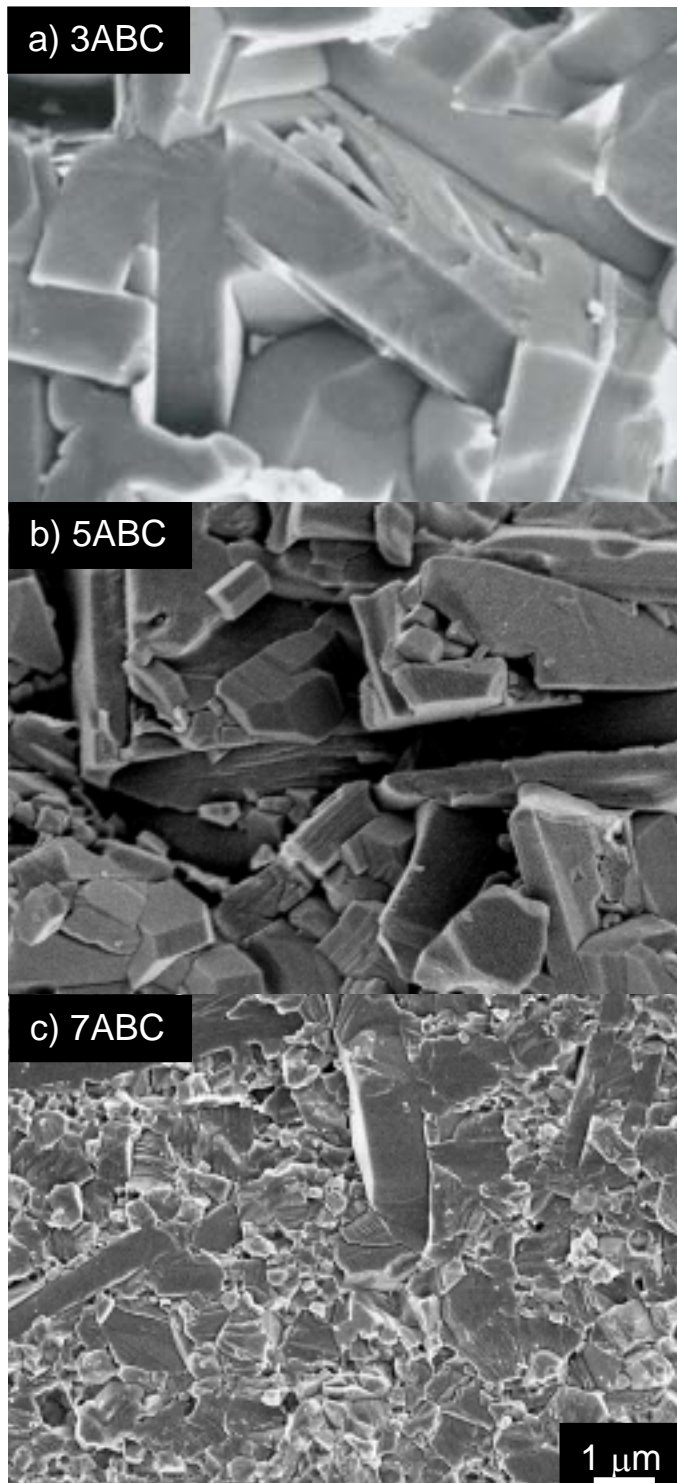


Fig. 2.5. SEM micrographs of the overload fracture surfaces of (a) 3ABC-, (b) 5ABC- and (c) 7ABC-SiC. Fracture in 3ABC and 5ABC is intergranular, whereas it is predominantly transgranular in 7ABC.

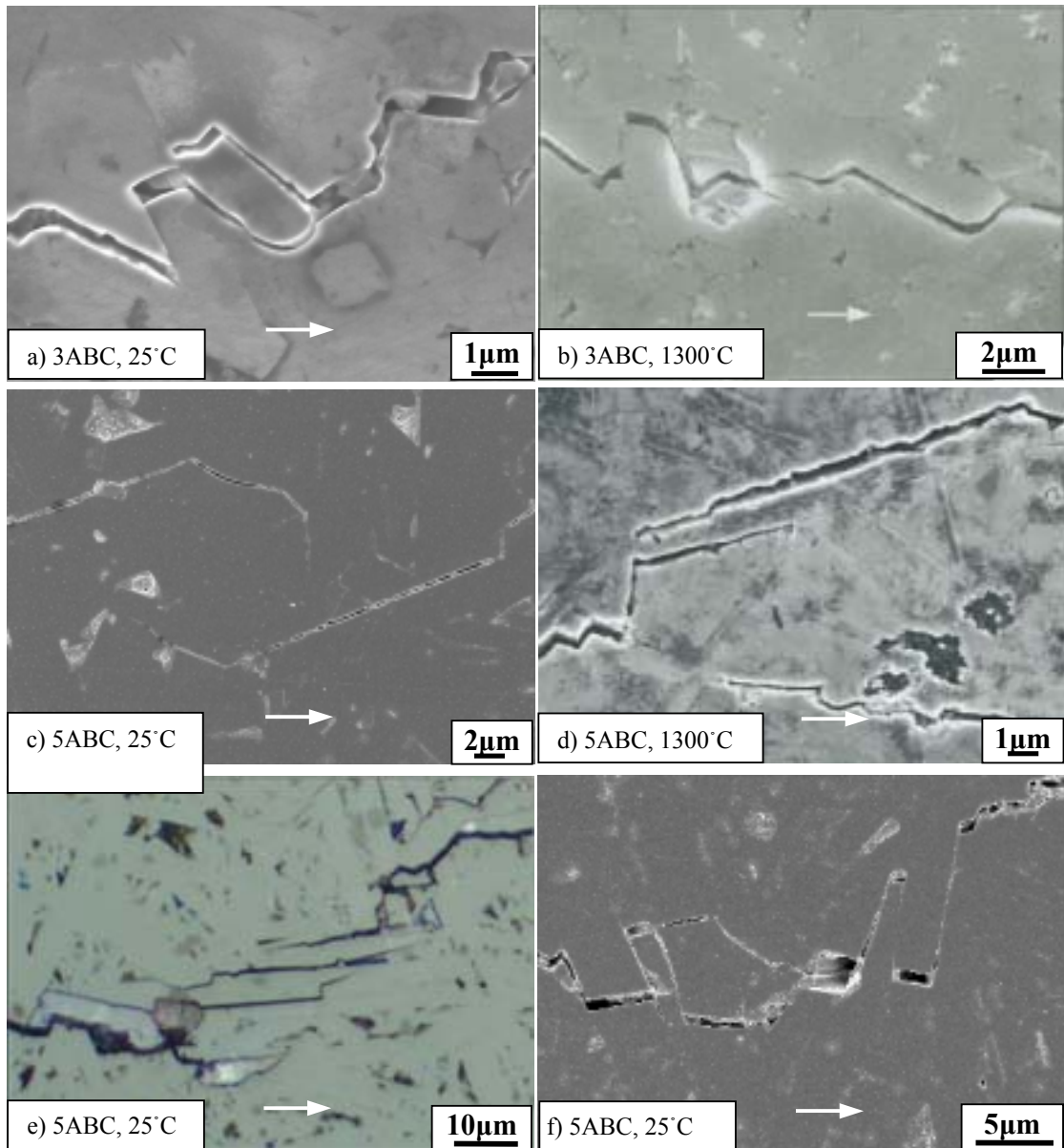
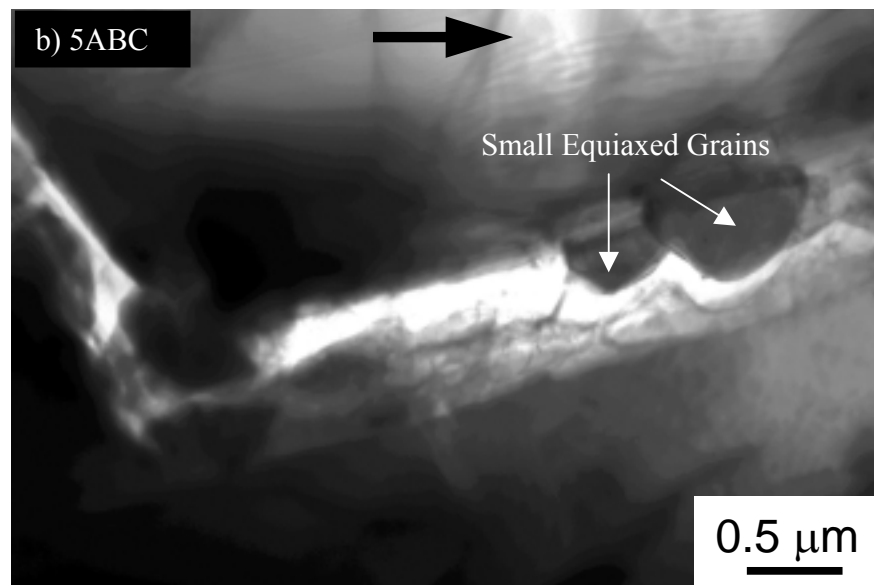
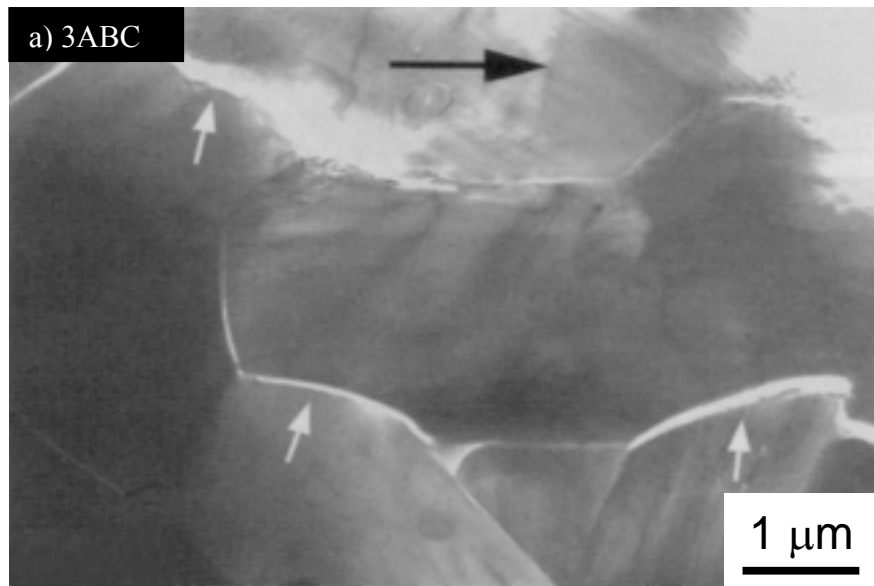


Fig. 2.6. SEM micrographs of metallographic sections taken perpendicular to the fracture surface showing the crack paths during fatigue-crack growth at 25°C and 1300°C for 3ABC (a,b) and 5ABC-SiC (c-f). Frictional bridging (a,b,f) was most common in 3ABC while uncracked ligament bridges (c,d,e) were predominant in 5ABC. The horizontal arrows indicate the general direction of crack growth.



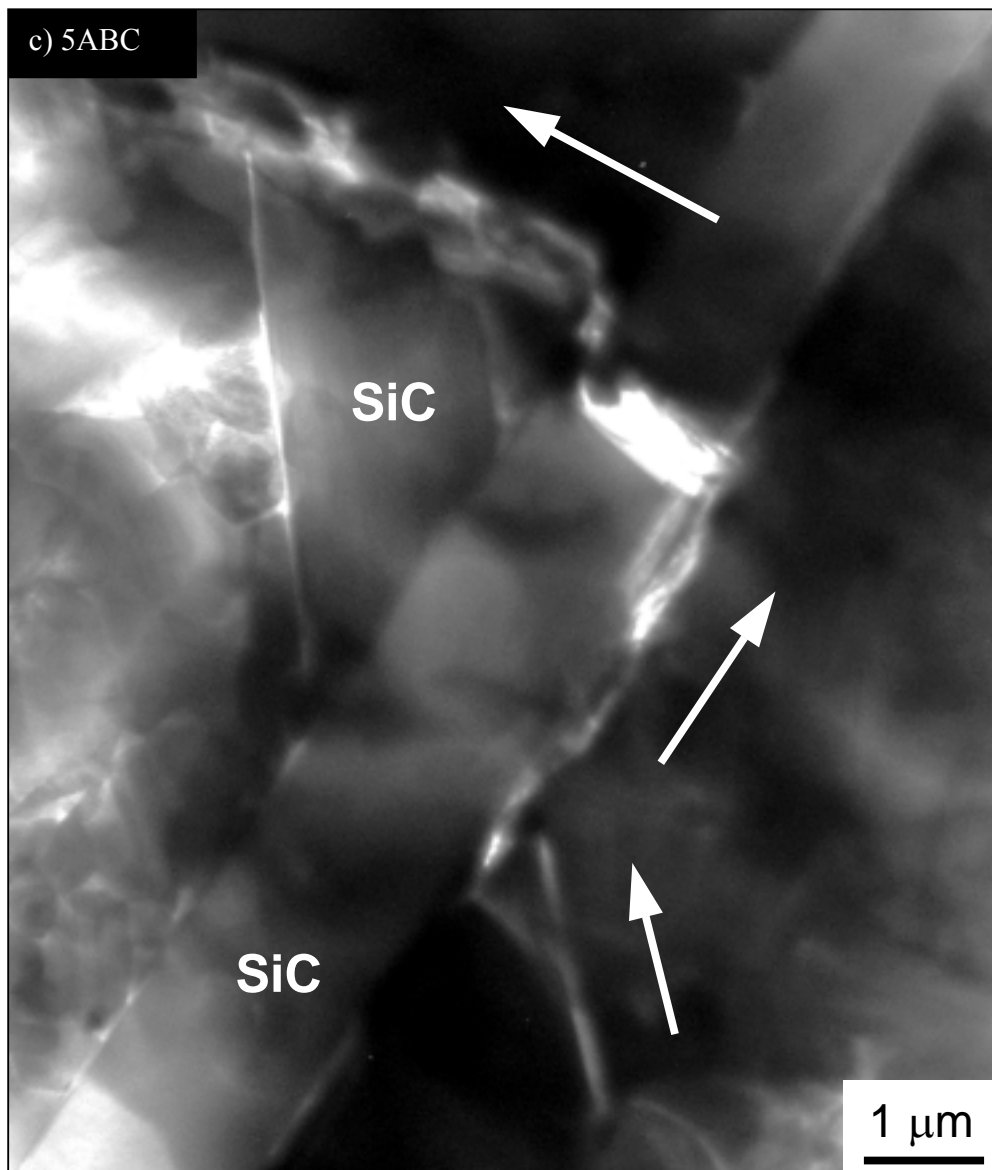


Fig. 2.7. Transmission electron micrographs near the crack tip in (a) 3ABC, and (b, c) 5ABC grown under cyclic loading at 1300°C ($R = 0.1$, $\nu = 25$ Hz). Note in (b) the equiaxed grains also fracture intergranularly and in (c) a failure of uncracked ligament. Large arrows indicate the general direction of crack propagation, and small arrows point to the primary cracks near the crack tip. (Courtesy of Dr. Xiao-Feng Zhang)

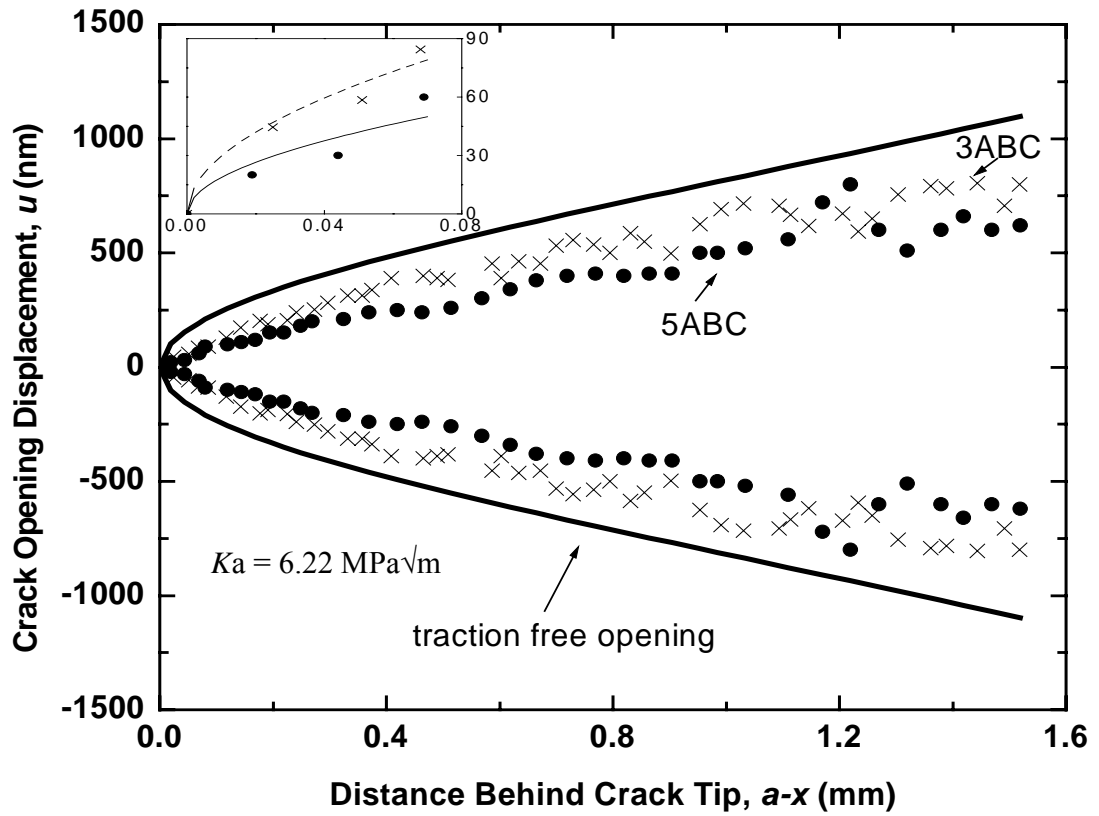


Fig. 2.8. Comparison of the crack-opening profiles for a monotonically-loaded crack in the 3ABC and 5ABC microstructure after R-curve testing. Samples were loaded *in situ* in a field-emission FESEM to an applied driving force of $6.2 \text{ MPa}\sqrt{\text{m}}$. The inset shows the curve fit for the first $70 \text{ }\mu\text{m}$ behind the crack tip, where the solid line is for 5ABC ($K_{\text{tip}}=1.6 \text{ MPa}\sqrt{\text{m}}$), and the broken line for 3ABC ($K_{\text{tip}}=2.5 \text{ MPa}\sqrt{\text{m}}$).

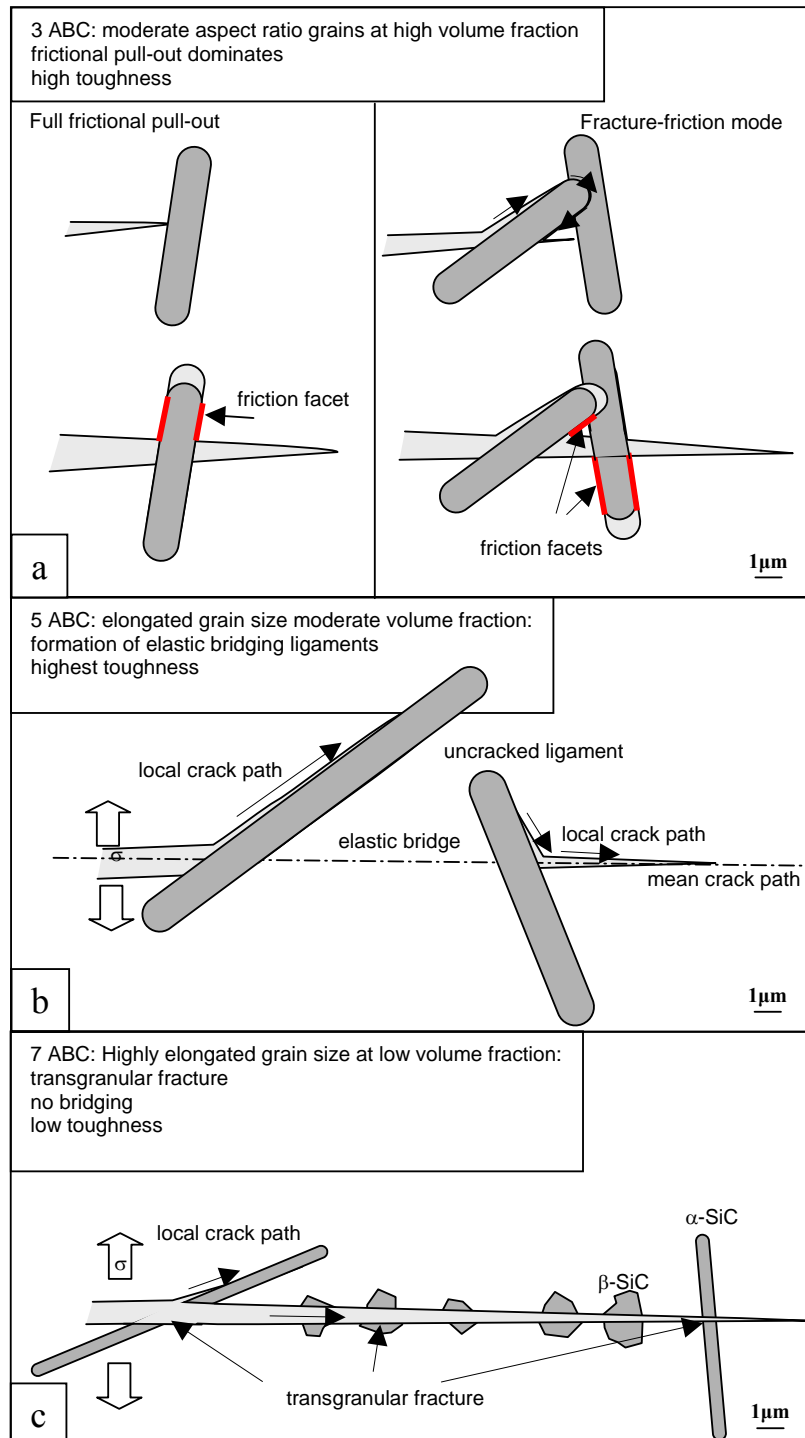


Fig. 2.9. Schematic illustrations of how the crack paths lead to the development (or not) of crack bridging in (a) 3ABC, (b) 5ABC, and (c) 7ABC-SiC. Note how the predominant mode of bridging in 3ABC is from frictional grain bridging, whereas it results more from uncracked ligaments in 5ABC; in contrast, no bridging is developed in the 7ABC. (Courtesy of Prof. De Jonghe).

CHAPTER 3

A GRAIN BRIDGING MODEL FOR NON-TRANSFORMING CERAMICS

3.1 REVIEW OF GRAIN BRIDGING MODELS

Subcritical crack extension in ceramics has received much attention since the 1960s. Before grain bridging was identified as a principal mechanism associated with such subcritical crack growth, microcracking was believed to be the main reason for the behavior of rising resistance with crack size (R-curve) in non-transforming ceramics. In 1977, Hubner and Jillek [1] first compared the R-curve behavior of alumina (Al_2O_3) specimens with sharp cracks and blunt notches and found that phenomena in the crack wake is mainly responsible for the increased toughness. Five years later, Knehans and Steinbrech evaluated R-curve behaviors of Al_2O_3 at different notch lengths and confirmed that this rising R-curve behavior is only associated with crack wake phenomena [2]. However, the primary toughening mechanism for many non-transforming ceramics remained somewhat unclear until Swanson *et al* [3] in 1987 directly observed the microstructural features in the crack wake of toughened alumina by scanning electron microscopy (SEM), precluding the previously assumed microcracking mechanism. Based on their results, Mai and Lawn [4] first proposed a grain bridging toughening mechanism by introducing the concept of a compressive bridging stress which arises from the zone of interlocking grains behind the crack tip. This reduces the stress intensity factor experienced at the crack tip, thereby requiring additional external work to be done for the crack to grow which in turn causes the rising behavior of the resistance curve.

Since that time, numerous studies [3-28] have attempted to develop an understanding of this mechanism from two different aspects, namely, quantification of

the bridging stress and R-curve behavior and the specific role of microstructure. With respect to the issue of microstructure, several different explanations have been proposed for the physical origins of compressive bridging stresses and micromechanics-based constitutive laws formulated to provide a quantitative description of the effect of microstructure features (e.g., grain size, grain structure and grain boundaries) on the bridging stress and R-curve behavior. With respect to quantification of the bridging effect, several techniques have been developed, including crack profile measurements, multi-cutting compliance experiments and post fracture tensile tests, which provide ways to quantify the bridging stress, as well as the shape of the resistance curve from the initial toughness to the final plateau. A brief review of the development of the grain bridging mechanism based on these two aspects is given below.

3.1.1 Microstructural Aspects

3.1.1.1 Bridging Forms and Micromechanics-based Constitutive Law

Experimental observations of the crack wake of ceramics toughened by the grain bridging mechanism suggest that there are three main processes by which energy is dissipated at the crack surfaces: (i) debonding or bending of elastic bridging ligaments, (ii) frictional pullout of the debonded grains, and (iii) rotation of bridged grains trapped in sockets of the matrix [9,15]. Because different bridging processes correspond to different constitutive laws, the main process determines how the constitutive law is constructed. Some studies [4,15,17] have claimed that frictional bridging dominates the toughness increase, based on theoretical estimates of the energy dissipated by each bridging process; these studies also conclude that the role of friction is most prevalent in the crack wake. Others [20] conclude that the

debonding process is the primary source for toughening based on measurements of the bridging stresses along the crack surfaces in silicon nitride (Si_3N_4).

Although the dominant bridging process is still in debate, the most commonly used constitutive law [4] to determine the bridging stress p , is the one used for the frictional pullout of grains:

$$\begin{aligned} p(x) &= \mu\sigma_N \left(1 - \frac{u}{u_{\max}}\right)^n \\ &= \mu\sigma_N \left(1 - \frac{a-x}{L}\right)^n \end{aligned} \quad (3.1)$$

where σ_N is the clamping stress that the matrix applies on the bridged grain, μ is the friction coefficient, u is half the crack opening displacement inside the bridging zone, u_{\max} is half the maximum crack opening displacement at the end of the bridging zone, n is a shape factor which determines how fast the bridging stress decays with the increase of the crack opening displacement, a is the crack length, x is the position along the crack surface, $a-x$ is the distance behind the crack tip, and L is the bridging zone length. Based on experimental observations that the crack profile is closer to linear than parabolic [10], the constitutive law can also be written in terms of the distance behind the crack tip, $a-x$, with the same shaper factor by assuming a straight crack profile [11,12].

Later Bennison and Lawn [9] revised the constitutive law to include a contribution from elastic bridging in addition to frictional bridging; they also considered microstructural parameters such as average grain size and shape, grain boundary, residual stresses and friction coefficients. Since their complex model did not employ the power law form (Eq. 3.1), but instead assumed a linear dependence of the bridging stress on the crack opening displacement, which conflicts with most experimental results [10,11,21,25,29,30], Sohn *et al.* [6] modified Bennison's model by including a

grain size distribution to make the overall stress-displacement relationship non-linear. Although Bennison's model included many useful features such as microstructural parameters, it was too complicated to use. Accordingly, most subsequent studies on the quantification of bridging stresses and R-curve behavior have employed the simple power-law form for the bridging stresses and displacements.

3.1.1.2 Physical Origin of the Bridging Stress

In the frictional bridging mechanism, the bridging stress is considered to result from the friction generated between the bridged grains and the matrix. The "clamping" stress on the boundaries was believed to originate from thermal expansion anisotropy associated with quenching from a high temperature during processing of non-cubic structures [9]. However, grain bridging also exists in MgAl_2O_4 spinel ceramics [7,30,31], where no such thermal mismatch exists owing to its cubic structure. This implies that a universal source for the clamping stress may exist independent of the crystal structure. Indeed, it is now thought that it is associated with the mechanical interlocks caused by the rotation and jamming of the grains [15]. In summary, there are two sources of the clamping stress for frictional bridging: the general mechanical interlock and the thermal anisotropy mismatch seen only in non-cubic structures following high temperature processing.

3.1.1.3 The Effects of Microstructure on Bridging Stresses and R-curves

A) Grain Size and Distribution. In Bennison and Lawn's proposed constitutive law [9], the maximum bridging stress for frictional pullout is inversely proportional to the grain size, but this relationship has never been proven experimentally. Contrary to the intuitive belief that the bridging zone length should be proportional to the grain size, Vekinis' work in Al_2O_3 [15] showed the opposite trend. It is still not clear whether this trend is true irrespective of material because there has not been any

systematic study to examine this point. However, there is general agreement on the effect of grain size on R-curve behavior; in general, the toughness increases with grain size [15,32] because the frictional pullout occurs over larger distances in the crack wake [14,19]. Yet grain size alone does not determine the toughness; recent work on Si_3N_4 [19] and ABC-SiC [25] has shown that a bimodal grain structure can optimize the toughness properties.

B) Grain Shape. Elongated grains have been shown to result in a marked increase in the toughness compared to equiaxed grain structures [17,19,24,25]. The reason for this trend lies in two facts: more extensive bridging can be formed, and the frictional resistance increases due to an extra clamping stress from the thermal anisotropic mismatch during processing.

C) Grain Boundary. The state of the grain boundaries, e.g., the presence of a second phase or intergranular film, will not only affect the frictional coefficient [24-26,33] in Eq.(3.1), but also influence the interfacial debonding [19,23,25,34]; it can even change the dominant bridging mechanism [25]. Recent studies on ABC-SiC showed that for the same material, crystallization of the grain boundary films increased the fracture toughness [24-26,33], which might be due to an increase in the frictional coefficient; for a series of Al-containing SiC, the partially crystalline and partly amorphous grain boundaries promoted the formation of unbroken ligaments (elastic bridging). The role of the grain boundary is not fully understood and more work needs to be done to understand its influence on the interfacial debonding.

3.1.2 Quantification of Bridging Stress and R-curve Behavior

The shape of R-curve is important since it shows the relationship between toughness, flaw size, and strength [9,35], which is invariably the basis for actual design and application. Usually the intrinsic toughness and the initial rising part of

the R-curve are difficult to obtain from direct measurements, so various experimental techniques and theoretical models have been developed to determine the initial toughness and the shape of the resistance curve. These involve determining the bridging stress either from direct measurement or a combination of experiments and numerical fitting. To date, several types of quantification techniques have been proposed, as briefly discussed below.

3.1.2.1 Integral of bridging stress by LEFM

In LEFM, the linear superposition for displacement fields, stress fields, and stress intensity factors can be achieved simultaneously and they are related to each other by so-called weight functions [36,37]. There are three stress intensity factors that need to be considered for loaded ceramics, namely, the applied stress intensity factor K_{App} arising from the externally applied loads, the bridging stress intensity factor K_b arising from the internal compressive bridging stresses, and the intrinsic stress intensity factor K_{In}^* associated with the material resistance in the absence of bridging. Usually only the applied stress intensity factor can be obtained from experiments. In order to obtain both the initial and bridging stress intensity factors, the bridging stress needs to be known, from which the bridging stress intensity factor can be calculated through the integral of bridging stress and the weight function. One way to quantify the bridging stress is to directly measure it along the crack surfaces using either fluorescence or Raman spectroscopy [20,22]; alternatively, the crack opening displacement (COD) can be measured and parameters fitted for a presumed bridging stress function [8,10,16,21]. Once the bridging stress function is known, the reduced stress intensity factor from bridging is obtained from the integral of the bridging stress with the weight function. Some studies [10,20,21] have specifically employed the

* The intrinsic stress intensity factor K_{tot} is the total effect of the externally applied stress intensity factor and the internal bridging stress intensity factor. Form linear superposition theorem in LEFM, $K_{tot} = K_{App} - K_b$

Barenblatt relation, which is indeed a special case of the weight function method (Appendix 3.1).

3.1.2.2 Cutting Compliance

In 1991, Hu *et al.* [11,12] developed the compliance cutting method to determine the bridging stress distribution along the crack path. This experiment is based on the concept that the existence of the bridging causes a decrease in compliance, and the gradual removal of the bridged grains by saw-cutting finally brings the compliance back to its bridging-free value. Thus, the bridging stress can be evaluated from the change of compliance with notch length. Key to this theory are (i) that the measurement of compliance is conducted at a fixed displacement, and (ii) that the assumption that the bridging stress decreases with external load at a constant ratio for each removal. This measurement does not rely on an assumption of linear elasticity or linear crack profiles, but is limited by the amount of cutting between each measurement interval. They further added the assumption of linear crack profile and power-law bridging stress form (Eq. 3.1) to obtain the stress magnitude from the measured toughness [11]. Recently, Kruzic *et al.* [28] combined this method with the COD method for LEFM conditions. They used the compliance cutting technique to determine the bridging stress distribution, and then used COD to determine the bridging stress magnitude from regression analysis. Stress intensity factors are calculated through the weight function.

3.1.2.3 J-integral approach

Steinbrech *et al.* [14] used the energy approach to quantify the toughness increase resulted from grain bridging:

$$J_b = J_{wake} = 2 \int_{x^*}^a \sigma_b(u(x)) \frac{du(a,x)}{da} dx \quad (3.2)$$

where toughness increase from bridging is the J -integral along the crack wake, $\sigma_b(u(x))$ is the bridging stress acting on the crack surfaces, $u(a,x)$ is the half crack opening displacement, a is the crack length, and x^* is the position at the end of the bridging zone. These authors measured the entire R-curve, used Eq.(3.1) in the form of the bridging stress leaving the shape factor, n , to be determined, obtained $\frac{du(a,x)}{da}$ from experiments, and then did numerical fitting for n to get the bridging stress for their experimentally-tested material.

3.1.2.4 Post Fracture Tensile Test (PFT)

Rather than taking the empirical bridging stress function in Eq.(3.1) for granted, Hay and White [7,30] developed the post fracture tensile test to obtain the bridging stress. They prepared tensile specimens with a through-width crack and the specimens were only connected by the bridged grains. Then they performed tensile tests and recorded the load-displacement curves for different crack openings, from which a stress-displacement curve for the bridging stress behavior was constructed. **By** this approach, the energy dissipated by bridged grains was calculated using:

$$G_b = \frac{1}{a} \int_{x^*}^a \int_0^{\delta(x)} \sigma_b(\delta) d\delta dx \quad (3.3)$$

where δ is the full crack opening displacement, and other terms are the same as in Eq.(3.2)

The problem with this approach is that firstly, the load-displacement that they measured at the load point is not the same as that at the crack opening since the material is deformable; secondly, they could not obtain the stress-displacement relationship at very small crack openings. Later Fett *et al.* [27] corrected the measurement by using a laser interferometer displacement gauge to measure the displacement of the bridged crack, and used the weight function from LEFM to

construct from R-curve measurement the stress-displacement relation for small crack openings. The bridging stress function that they obtained had a peak stress, combining the effects of elastic bridging and frictional pullout, just as described by Bennison [9].

3.1.2.5 Work loop combined with frictional model

This model was developed by Vekinis *et al.* [15] and is different from the previous four techniques which all deal with the bridging stress. This model incorporates experiments involving the loading-unloading curve with the real physical process of frictional bridging. It equated the loop of external work done to the toughness increase just after the crack “pop-in”, and cannot be combined with LEFM since it assumes work done even during unloading.

3.2 PROPOSED LEFM GRAIN BRIDGING MODEL

To date, however, the analytical models based on linear elastic fracture mechanics (LEFM) that have been used have not always been clearly stated, and in certain cases, the relationship between the stress intensity factor and the material fracture resistance have been incorrect [10]. Therefore, our goal is to provide an analytical model using LEFM to quantify the fracture properties from measured quantities, and to relate the stress intensity factors to the fracture resistance. This model is based on Mai and Lawn’s assumptions about bridging stresses [4], as well as the experimental results by Hubner and Jillek, and Knehans and Steinbrech [1,2,14]. Then the linear superposition theorem and weight functions are used to derive the expression of fracture resistance in terms of stress intensity factors which correspond to their loading origins as mentioned in section 3.1.2.1. Finally an experimental procedure is proposed to obtain the fracture properties based on the analysis.

3.2.1 Prerequisites

Three prerequisites are needed to formulate the analytical model for the grain bridging mechanism in non-transforming ceramics: the idealization of the compressive bridging stress from the microstructure from Mai and Lawn's work [4], the use of LEFM, and the separation of the fracture resistance based on Knehans and Steinbrech's experiments [2,14].

First, for the bridging stress, three assumptions are made [4]: 1) The crack with discrete bridging events is idealized as one with continuous compressive stresses acting on its surfaces [4,14]. In addition, the bridging stress is taken to only exist over a finite interval, from the crack tip to some place along the crack surface. 2) The bridging stress is a function of the distance behind the crack tip $a-x$, written as $\sigma_b(x)$, as well as a function of crack opening displacement, $\sigma_b(u)$, provided that there exists a relationship between the position and the crack opening displacement, $u(x)$. Also at the end of the bridging zone, the bridging stress is zero. 3) The bridging stress simply translates with the crack, as a function of the distance behind the crack tip (Fig. 3.1), and the bridging zone length is a function of the crack length, a , given by:

$$L(a) = \begin{cases} a - a_N, & a < a_N + L \\ L, & a \geq a_N + L \end{cases} \quad (3.4)$$

where a_N is the length of the notch, and L is the length of a fully developed bridging zone length. Thus, the constitutive law for bridging stress has the form:

$$\begin{aligned} \sigma_b(x) &= \Sigma(a-x, L(a), \dots) \\ \sigma_b &= 0, \text{ at } x \leq a-L \end{aligned} \quad (3.5)$$

Second, in linear elastic fracture mechanics, the superposition theorem (Fig 3.2) and the weight function are used to relate the bridging stress to COD and stress intensity factors. The superposition for CODs and stress intensity factors are as given in Eqs. (3.6a) and (3.6b).

$$u_{eff}(x) = u_{App}(x) - u_b(x) \quad (3.6a)$$

$$K_{eff}(a) = K_{App}(a) - K_b(a) \quad (3.6b)$$

where K_{App} is the applied stress intensity factor caused by the external loading, K_b is the bridging stress intensity factor arising from the internal compressive bridging stresses generated by the interlocking bridging zone, and K_{In} is the effective stress intensity factor at the crack tip which actually controls the crack propagation process. Also u_{In} , u_{App} and u_b are half the crack opening displacement in the test piece containing a crack of length a , resulting from K_{In} , K_{App} and K_b , respectively. Then, by the weight function, the crack opening displacements from each stress intensity factors are given by:

$$u_\gamma(x, a) = \frac{1}{H} \int_0^a K_\gamma(a') h(x, a') da', \quad \gamma = In, App, b \quad (3.7)$$

In addition, the stress intensity factors K_{App} and K_b are related to the external traction (without body force) and the internal bridging stress by the weight function as:

$$K_{App}(a) = \int_\Gamma \underline{t} \cdot \underline{h}(\underline{x}, a) ds \quad (3.8a)$$

$$K_b(a) = \int_{a-L(a)}^a h(x, a) \sigma_b(x) dx \quad (3.8b)$$

where \underline{t} is the traction acting on boundary Γ , $\underline{h}(\underline{x}, a)$ is the weight function in vector form, and $h(x, a)$ is the weight function only along the crack surfaces. For most of the ASTM standard specimens, the applied intensity factor is calculated from the external load and geometry of the specimen (the thickness B , the width W , and the geometric function $f(a/W)$).

$$K_{App}(a) = \frac{P}{B\sqrt{W}} f(a/W) \quad (3.9)$$

Third, the separation of the fracture resistance is based on the ‘‘renotch’’ experiments conducted by Knehan and Steinbrech *et al.* [2,14], whose work indicates

that the initial toughness at the end of the crack notch is independent of the notch length (Hubner and Jillek's work [1] also showed this.) and the toughness increase comes only from the crack wake. Therefore, the apparent fracture resistance, R_A , evaluated from the external load and corresponding displacement is separated into two terms [14]: the extrinsic toughness increase, R_b , from the crack wake due to bridging, and the initial (or intrinsic) toughness, R_{In} , whose value is evaluated at the end of the notch and is a constant:

$$R_A(a) = R_{In} + R_b(a) \quad (3.10)$$

One assumption that is made is that the intrinsic toughness is related to the effective stress intensity factor, K_{In} , by the square relationship given by:

$$R_{In} = G_{In} = \frac{K_{In}(a)^2}{H} \quad (3.11)$$

Hence, $K_{In}(a)$ is also a constant, independent of the crack length [10].

Fig 3.3 shows the relationship among the traction on the boundary, the resultant displacements, the stress intensity factors, together with the critical crack driving force (or material fracture properties), for a quasi-static crack propagation process in a linear elastic material. The displacements, loading, and the stress intensity factors are related to each other by the weight function in LEFM; the material resistance is derived from the virtual work calculated from loading and the resultant displacements. However, the relationship between the material resistance and the stress intensity factors is unknown.

3.2.2 Critical Crack Driving Force and the Material Resistance

With the above background, the material resistance or the critical crack-driving force for ceramics toughened by the grain bridging mechanism is evaluated using the potential energy in LEFM and the Clapeyron theorem for quasi-static crack

propagation. Our goal is to relate the apparent fracture resistance $R_A(a)$ and the toughness increase due to bridging $R_b(a)$ to the effective stress intensity factor K_{In} , externally applied stress intensity factor K_{App} and internal bridging stress intensity factor K_b .

Consider a symmetric two-dimensional linear elastic structure with a crack under a symmetric external loading and internal bridging stresses on the crack surfaces. A simply-connected closed contour is selected along the boundary (Fig. 3.4) (crack surfaces are considered as part of the boundary) of the body, on which the virtual work is evaluated. Then the critical crack driving force for the linear elastic body is given by (Appendix 3.2, Eq. (A3.14)):

$$R_{In} = G_{In} = \frac{K_{In}^2}{H} = \frac{1}{2} \frac{dV}{da} \Big|_{\text{fixed loading}} \quad (3.12)$$

In equation (3.12), the virtual work, V , consists of two parts: V_{ex} from the externally applied traction on the contour Γ_{ex} , and V_b from the internal bridging stress on Γ_b (crack opening displacement is so small that $ds=dx$):

$$\begin{aligned} V &= V_{ex} + V_b \\ &= \int_{\Gamma_{ex}} \underline{t} \cdot \underline{u} ds - \int_{\Gamma_b} \sigma_b(a-x) u_{In}(x,a) ds \\ &= V_{ex} - 2 \int_{a-L(a)}^a \sigma_b(a-x) u_{In}(x,a) dx \end{aligned} \quad (3.13)$$

Putting Eq.(3.13) in to (3.12) and rearrange the equation, we get

$$\underbrace{\frac{1}{2} \frac{\partial V_{ex}}{\partial a} \Big|_{\text{fixed loading}}}_{(1)} = \frac{K_{In}^2}{H} + \underbrace{\frac{\partial \left\{ \int_{a-L(a)}^a \sigma_b(a-x) u_{In}(x,a) dx \right\}}{\partial a} \Big|_{\text{fixed loading}}}_{(2)} \quad (3.14)$$

Clearly, the term (1) is the contribution from externally applied traction, whereas term (2) is the contribution from grain bridging. Thus, we define term (1) as the apparent

material resistance, $R_A(a)$, and term (2) the toughness increase from the bridging $R_b(a)$.

After further simplification by Leibnitz rule, $R_b(a)$, becomes:

$$\begin{aligned} \text{Term (2)} &= \int_{a-L(a)}^a \sigma_b(x) \frac{\partial u_{in}(x, a)}{\partial a} dx + \sigma_b(a) u_{in}(a, a) \\ &\quad - \sigma_b(a-L(a)) u_{in}(a-L(a)) (1-L'(a)) \end{aligned} \quad (3.15)$$

Recall that from Eq.(3.4), when $a < a_N + L$, $1-L'(a)=0$; and when $a > a_N + L$, $\sigma_b(a-L(a))=0$.

Also at the crack opening displacement at the crack tip is zero, i.e., $u_{in}(a, a)=0$. Thus,

only the first part in term (2) is nonzero. Combining term (2) and the weight function

Eq.(A3.1), we get:

$$\begin{aligned} \text{Term (2)} &= \int_{a-L(a)}^a \sigma_b(x) \frac{\partial u_{in}(x, a)}{\partial a} dx \\ &= \int_{a-L(a)}^a \sigma_b(x) \frac{K_{In}}{H} h(x, a) dx \\ &= \frac{K_{In} K_b(a)}{H} = R_b(a) \end{aligned} \quad (3.16)$$

Thus, term (1) or $R_A(a)$ in Eq.(3.14) reduces to:

$$R_A(a) = \frac{1}{2} \frac{\partial V_{ex}}{\partial a} \Bigg|_{\substack{\text{fixed} \\ \text{loading}}} = \frac{K_{In} K_{App}(a)}{H} = G_{App}(a) \quad (3.17)$$

3.2.3 Proposed experimental procedure to obtain the material resistance and the stress intensity factors

Based on Eq.(3.14) we propose a method to measure $R_A(a)$ and R_{In} using standard ASTM specimens (Fig.3.5a). First, the external load, the load-point displacement, and the measured crack size[†] are recorded (Fig.3.5b). Then the virtual work and the stress intensity factor from the externally applied load ($V_{ex}(a)/2$ and $K_{App}(a)$) are calculated using Eqs. (A3.15a) and (3.9) respectively, and plotted against crack length (Figs. 3.5 c and e). The derivative of half the external virtual work, $V_{ex}(a)/2$, with respect to a is

[†] The crack length cannot be measured by the compliance method, since the existence of the bridging changes the compliance. The crack length can be measured by telescope or other techniques that do not use the compliance.

calculated in order to get the apparent fracture resistance $R_A(a)$ (Fig.3.5 d). Finally, according to Eq.(3.17), the linear regression of $R_A(a)$ and $K_{App}(a)$ give the slope, K_{tot}/H . Consequently, R_{In} , $K_b(a)$ and $R_b(a)$ are obtained by Eq.(3.12), (3.6b) and (3.10).

For the above procedure, three issues need to be noted. Firstly, the crack does not need to grow exactly from notch; only part of the resistance curve, as well as the applied stress intensity curve, can determine the initial toughness. Secondly, the form of the bridging stress is not specified. Thirdly, although the initial toughness value can be determined, the full shape of the resistance curve is still unknown from this experimental procedure; thus other experimental techniques or a micromechanics-based constitutive law (as stated in section 3.1) are needed to determine the shape of the R-curve. For example, if the bridging stress $\sigma_b(x)$ is assumed to take the form of Eq.(3.1), then the parameters in it can be obtained from partial curve of $K_b(a)$ through Eq. (3.8b) by regression fitting. With the bridging stress function known, the full shape of $K_b(a)$ is obtained, hence other properties are known, such as the complete rising R-curve.

3.2.4 Discussion

(1) *Bridging Stress.* In this work, the micromechanics-based constitutive law for bridging stress uses the distance behind the crack tip as an internal variable (Eq. 3.5) and bridging stress simply translates with crack extension. Since no assumption of the linear crack profile is made, this theoretical derivation allows for all kinds of crack profiles.

(2) *Apparent fracture resistance, $R_A(a)$.* From Eq.(3.17), the apparent fracture resistance is less than K_{App}^2/H because the internal compressive bridging stress restrains the displacements caused by the external tractions.

(3) *Effect of sample size on $R_b(a)$.* Also from Eq.(3.8b), it is clear that the increased toughness may become sample size dependent if the bridging zone length is comparable to the crack size. Since some researchers reported a very large bridging zone length in their tests [33], some concern is warranted: for example, will the bridging zone length increase with sample size? If so, does it increase linearly with the structure size? If the bridging zone length is independent of the sample size, then what is the critical sample size above which the measured toughness can be applied to structures of different sizes? So far no experiments have been performed to investigate these issues.

3.3 CONCLUSIONS

(1) The fracture resistance and stress intensity factors for external loading $K_{App}(a)$, internal bridging stresses K_b , and crack initiation K_{In} , are formulated by linear elastic fracture mechanics. Linear superposition theorems and the weight function are used to relate the CODs, stress intensity factors corresponding to their loading origins, namely, external tractions and the internal bridging stress. The apparent material resistance from the contribution of external loading is found to be $K_{In}K_{App}(a)/H$, the bridging resistance $K_{In}K_b(a)/H$, and intrinsic toughness a constant K_{In}^2/H , where H is Young's modulus E in plane stress condition, and $E/(1-\nu^2)$ in plane strain condition, and ν is the Poisson ratio.

(2) Experimental procedures to obtain the fracture resistance and stress intensity factors are proposed based on above results.

(3) Sample size may affect the measured toughness if the bridging zone length is comparable to the sample dimensions.

(4) All the results are based on linear elastic fracture mechanics. However, Vekinis' [15] experiments on alumina ceramics showed that the net work done is not zero in a loading-unloading loop without crack extension, thus linear elastic fracture mechanics is not totally applicable. Further analysis is needed to quantify the fracture properties from the experiments.

APPENDIX 3.1

WEIGHT FUNCTION AND THE BARENBLATT MODEL

In linear elastic fracture mechanics, the weight function for a symmetric geometry under symmetric loading is unique [37], and independent of loading distribution. With the x-axis coincident with the crack, the Mode I weight function along the crack surface, $h_I(x, a)$, is defined as [8]:

$$h_I(x, a) = \frac{H}{K_I(a)} \frac{\partial u(x, a)}{\partial a} \quad (\text{A3.1})$$

where $u(x, a)$ is the crack opening displacement along the x-axis, a the crack length, $K_I(a)$ the stress intensity factor at crack length a , H is the Young's modulus, E , for plane stress and $E/(1-\nu^2)$ for plane strain, and ν is the Poisson ratio. Two applications for the weight function are shown in Eqs. (A3.2) and (A3.3): to obtain the stress intensity factor for a certain geometry under an arbitrary loading distribution, and to derive the crack opening displacement (Fig. 3.6).

$$K_I(a) = \int_0^a h_I(x, a) \sigma(x) dx \quad (\text{A3.2})$$

$$u(x, a) = \int_x^a h_I(x, a') K_I(a') da' \quad (\text{A3.3})$$

where $\sigma(x)$ is the traction acting on the crack surfaces. Combining (A3.2) and (A3.3), the displacement is expressed by a double integral form of weight function and stress function (Fig. 3.7) as:

$$\begin{aligned} u(x, a) &= \frac{1}{H} \int_x^a h(x, a') \left\{ \int_0^{a'} h(x', a') \sigma(x') dx' \right\} da' \\ &= \frac{1}{H} \int_0^a \sigma(x') \left\{ \int_{\max\{x, x'\}}^a h(x', a') h(x, a') da' \right\} dx' \end{aligned} \quad (\text{A3.4})$$

Since the weight function depends only on the geometry, the integral for crack opening displacement includes the effect of geometry. The weight function solutions at the crack surface can be found in Wu [38] or Fett's [39] book, and it is usually in the form given as follows:

$$h(x, a) = \underbrace{\sqrt{\frac{2}{\pi(a-x)}}}_{\text{weight function for infinite plate with an edge crack}} + \underbrace{\sqrt{\frac{2}{\pi a}} \sum_{(v, \mu)} \frac{A_{v\mu} \alpha^\mu}{(1-\alpha)^{3/2}} (1-\rho)^{v+1/2}}_{\text{geometric effects}} \quad (\text{A3.5})$$

where $\rho = x/a$, $\alpha = a/W$ and v, μ are dimensionless coefficients, which vary according to the geometry.

Conversely, Barenblatt's relation for the cohesive zone model is only valid for infinite plate containing a crack [40], which is a special case from the weight function method in LEFM:

$$u(x, a) = \frac{2}{\pi H} \int_0^a \sigma(x') \ln \left| \frac{\sqrt{a-x} + \sqrt{a-x'}}{\sqrt{a-x} - \sqrt{a-x'}} \right| \quad (\text{A3.6})$$

Equation (A3.7) shows that from the integral of weight functions, we can get Barenblatt relation (A3.6).

$$\begin{aligned} u(x, a) &= \frac{1}{H} \int_0^a \sigma(x') \left\{ \int_{\max\{x, x'\}}^a \sqrt{\frac{2}{\pi(a'-x')}} \sqrt{\frac{2}{\pi(a'-x)}} da' \right\} dx' \\ &= \frac{2}{\pi H} \int_0^a \sigma(x') \ln \frac{(\sqrt{a-x} + \sqrt{a-x'})^2}{|x-x'|} \\ &= \frac{2}{\pi H} \int_0^a \sigma(x') \ln \frac{(\sqrt{a-x} + \sqrt{a-x'})^2}{|(a-x) - (a-x')|} \\ &= \frac{2}{\pi H} \int_0^a \sigma(x') \ln \left| \frac{\sqrt{a-x} + \sqrt{a-x'}}{\sqrt{a-x} - \sqrt{a-x'}} \right| \end{aligned} \quad (\text{A3.7})$$

APPENDIX 3.2

ACTUAL WORK AND VIRTUAL WORK

One way to study fracture mechanics is to use the energy balance approach to quantify the material resistance to crack propagation in terms of energy. Before the quantification from the energy balance, three terms need to be interpreted: actual work, virtual work and strain energy. Actual work is the real work done to the body, given by the area under the load-displacement curve, whereas virtual work is simply the rectangular area determined by the final state of the load and the corresponding displacement (Fig. 3.8). The mathematical expressions for the actual work, W , the virtual work, V , and their increments due to the crack extension for the two dimensional case are given by:

$$W = \int_{\Gamma} \left[\int_0^{u_f} \underline{t} \cdot d\underline{u} \right] ds + \int_{\Omega} \rho \left[\int_0^{u_f} \underline{b} \cdot d\underline{u} \right] dA \quad (\text{A3.8a})$$

$$dW = \int_{\Gamma} (\underline{t} \cdot d\underline{u}) ds + \int_{\Omega} \rho (\underline{b} \cdot d\underline{u}) dA \quad (\text{A3.8b})$$

$$V = \int_{\Gamma} \underline{t}_f \cdot \underline{u}_f ds + \int_{\Omega} \rho \underline{b}_f \cdot \underline{u}_f dA \quad (\text{A3.9a})$$

$$dV = \left\{ \int_{\Gamma} \underline{t}_f \cdot d\underline{u} ds + \int_{\Omega} \rho \underline{b}_f \cdot d\underline{u} dA \right\} + \left\{ \int_{\Gamma} \underline{u}_f \cdot d\underline{t} ds + \int_{\Omega} \underline{u}_f \cdot d(\rho \underline{b}_f) dA \right\} \quad (\text{A3.9b})$$

Clearly, only when the crack propagates at a fixed load does the incremental virtual work equal the incremental actual work, i.e.,

$$dW = dV \Big|_{load}^{fixed} = dV \Big|_P \quad (\text{A3.10})$$

The third term that needs to be interpreted is the strain energy, U . It contains two parts: the elastic strain energy, U^{el} , which is completely recoverable upon removal of the load in an elastically unloading material, and the plastic strain energy, U^{pl} , which conversely, is non-recoverable during unloading.

In a quasi-static crack propagation process in elastically unloading materials (Fig. 3.9), the actual work done to a structure containing a crack is balanced by the strain energy of the body and the energy for crack extension. The net actual work done $E|_{loop}$ (area OA'B'C in Fig. 3.9) in a loading-unloading loop which causes the crack to grow from a to $a+\Delta a$, can be expressed as:

$$E|_{loop} = G_c \Delta a = R \Delta a = \Delta W_{a \rightarrow a+\Delta a} - \Delta U_{a \rightarrow a+\Delta a}^{el} \quad (A3.11)$$

So G_c is the critical crack driving force, also the material resistance, R is:

$$\begin{aligned} R = G_c &= \lim_{\Delta a \rightarrow 0} \frac{\Delta W - \Delta U^{el}}{\Delta a} \\ &= \frac{d(W - U^{el})}{da} = \frac{dV|_P - dU^{el}}{dx} \end{aligned} \quad (A3.12)$$

For a linear elastic load-bearing body in equilibrium, Clapeyron's theorem [41] shows that the virtual work is twice the elastic strain energy:

$$V = 2U^{el} \quad (A3.13)$$

So the material resistance or the critical crack driving force is further simplified to:

$$R = G_c = \frac{1}{2} \frac{dV}{da} \Big|_P \quad (A3.14)$$

For most of the ASTM specimens, the virtual work is simply the product of the load and its displacement:

$$V = P\Delta \quad (A3.15)$$

In LEFM, the fracture resistance is related to the applied stress intensity factors via weight function (Eq.(A3.14) and (A3.9a)):

$$\begin{aligned}
R(a) &= G_c = \frac{1}{2} \frac{dV}{da} \Big|_p \quad (A3.14) \\
&= \frac{1}{2} \left(\int_{\Gamma} \underline{t}_f \cdot \frac{\partial \underline{u}}{\partial a} ds + \int_{\Omega} \rho \underline{b}_f \cdot \frac{\partial \underline{u}}{\partial a} dA \right) \quad (A3.16) \\
&= \int_{\Gamma} \underline{t}_f \cdot \frac{K(a)}{2H} \underline{h}(\underline{x}, a) ds + \int_{\Omega} \rho \underline{b}_f \cdot \frac{K(a)}{2H} \underline{h}(\underline{x}, a) dA \quad (A3.9a) \\
&= \frac{K(a)^2}{H}
\end{aligned}$$

References

- [1] Hubner H, Jillek W. *Journal of Materials Science* 1977;12:117.
- [2] Knehans R, Steinbrech R. *Journal of Materials Science Letters* 1982;1:327.
- [3] Swanson PL, Fairbanks CJ, Lawn BR, Mai Y-W, Hockey BJ. *Journal of American Ceramics Society* 1987;70:279.
- [4] Mai Y-W, Lawn BR. *Journal of American Ceramics Society* 1987;70:289.
- [5] Fett T, Munz D, Thun G. *Journal of American Ceramics Society* 1995;78:949.
- [6] Sohn K-S, Lee S, Baik S. *Journal of American Ceramics Society* 1995;78:1401.
- [7] Hay JC, White KW. *Acta Metallurgy Materiala* 1992;40:3017.
- [8] Fett T, Munz D. *Journal of American Ceramics Society* 1994;77:3267.
- [9] Bennison SJ, Lawn BR. *ACTA METALLURGICA* 1989;37:2659.
- [10] Rodel J, Kelly JF, Lawn BR. *Journal of American Ceramics Society* 1990;73:3313.
- [11] Hu X-Z, Lutz EH, Swain MV. *Journal of American Ceramics Society* 1991;74:1828.
- [12] Hu X-Z, Wittmann FH. *Cement and Concrete Research* 1991;21:1118.
- [13] Wittmann FH, Hu X-Z. *International Journal of Fracture* 1991;51:3.
- [14] Steinbrech RW, Reichl A, Schaarwachter W. *Journal of American Ceramics Society* 1990;73:2009.
- [15] Vekinis G, Ashby MF, Beaumont PWR. *ACTA METALLURGICA ET MATERIALIA* 1990;38:1151.
- [16] Fett T, Munz D, Seidel J, Stech M, Rodel J. *Journal of American Ceramics Society* 1996;79:1189.
- [17] Gilbert CJ, Cao JJ, MoberlyChan WJ, De Jonghe LC, Ritchie RO. *Acta Metallurgy Materiala* 1996;44:3199.
- [18] Gilbert CJ, Cao JJ, De Jonghe LC, Ritchie RO. *Journal of American Ceramics Society* 1997;80:2253.
- [19] Becher PF, Sun EY, Plucknett KP, Alexander KB, Hsueh C-H, Lin H-T, Waters SB, Westmoreland CG. *Journal of American Ceramics Society* 1998;81:2821.
- [20] Pezzotti G, Muraki N, Maeda N, Satou K, Nishida T. *Journal of American Ceramics Society* 1999;82:1249.
- [21] Gilbert CJ, Ritchie RO. *Acta Materialia* 1998;46:609.
- [22] Pezzotti G, Sbaizero O, Sergio V, Muraki N, Maruyama K, Nishida T. *Journal of American Ceramics Society* 1998;81:187.
- [23] Sun EY, Becher PF, Plucknett KP, Hsueh C-H, Alexander KB, Waters SB. *Journal of American Ceramics Society* 1998;81:2831.
- [24] Chen D, Gilbert CJ, Zhang XF, Ritchie RO. *Acta Materialia* 2000;48:659.
- [25] Yuan R, Kruzic JJ, Zhang XF, DeJonghe LC, Ritchie RO. *Acta Materialia* 2003;51:6477.
- [26] Chen D, Sixta ME, Zhang XF, De Jonghe LC, Ritchie RO. *Acta Materialia* 2000;48:4599.
- [27] Fett T, Munz D, Dai X, White KW. *International Journal of Fracture* 2000;104:375.
- [28] Kruzic JJ, Cannon RM, Ritchie RO. *Journal of the American Ceramic Society* 2004;87:93.
- [29] Kruzic JJ, Yuan R, Cannon RM, Ritchie RO. *Materials Lifetime and Engineering*, TMS. Liaw PK, Buchanan RA, Klarstrom DL, Wei RP, Harlow DG, Liaw PK, Buchanan RA, Klarstrom DL, Wei RP, Harlow DG, Liaw PK, Buchanan RA, Klarstrom DL, Wei RP, Harlow DG. 2003,
- [30] Hay JC, White KW. *Journal of American Ceramics Society* 1993;76:1849.

- [31] Sakai M, Bradt RC, Kobayashi A. Journal of the Ceramic Society of Japan 1988;96:525.
- [32] Steinbrech RW, Knehans R, Scharwachter W. Journal of Materials Science 1983;18:265.
- [33] Chen D, Zhang XF, Ritchie RO. Journal of American Ceramics Society 2000;83:2079.
- [34] Becher PF, Hsueh CH, Alexander KB, Sun EY. 1996 1996;79:298.
- [35] Chantikul P, Bennison SJ, Lawn BR. Journal of American Ceramics Society 1990;73:2419.
- [36] Bueckner HF. Z. angew. Math. Mech. 1970;50:529.
- [37] Rice JR. International Journal of Solids and Structures 1972;8:751.
- [38] Wu X-R, Carlsson AJ. Weight functions and stress intensity factor solutions. Pergamon Press, 1991. p. 8.
- [39] Fett T, Munz D. Stress intensity factors and weight functions. Computational Mechanics Publications, 1997. p. 10.
- [40] Barenblatt GI. Advances in Applied Mechanics 1962;7:55.
- [41] Sokolnikoff IS. Mathematical theory of elasticity. McGraw-Hill, 1956. p. 86.

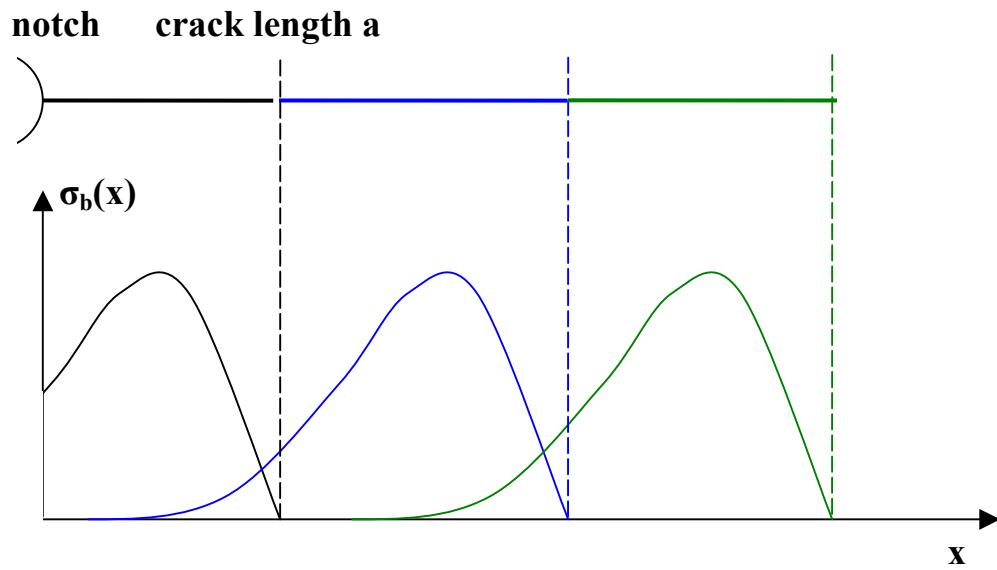


Fig. 3.1 Translation of the bridging stress with crack growth, based on Figure 2 in Ref. [4].

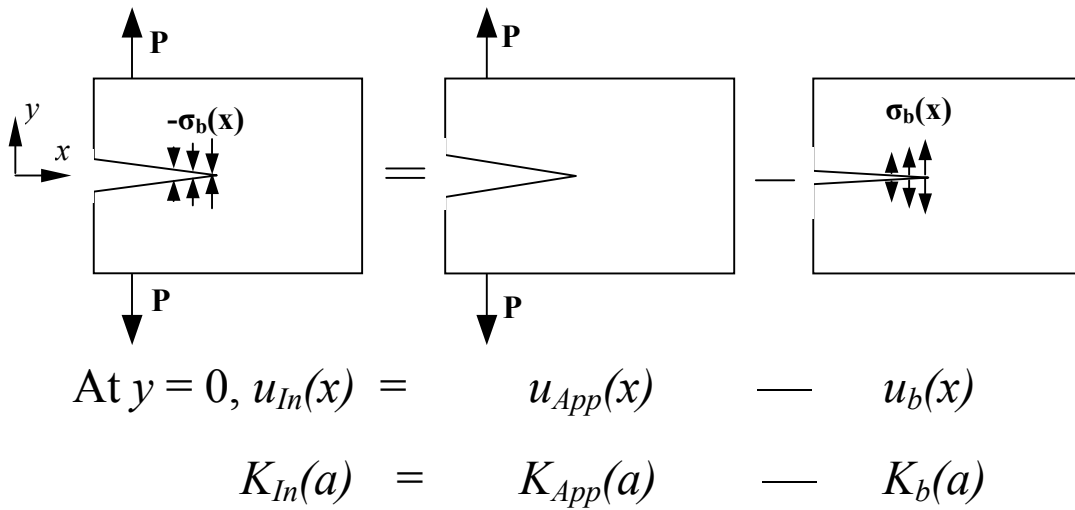


Fig.3.2. Linear superposition for crack opening displacements u and stress intensity factors K in the grain bridging model. The crack openings are exaggerated for the purpose of illustration.

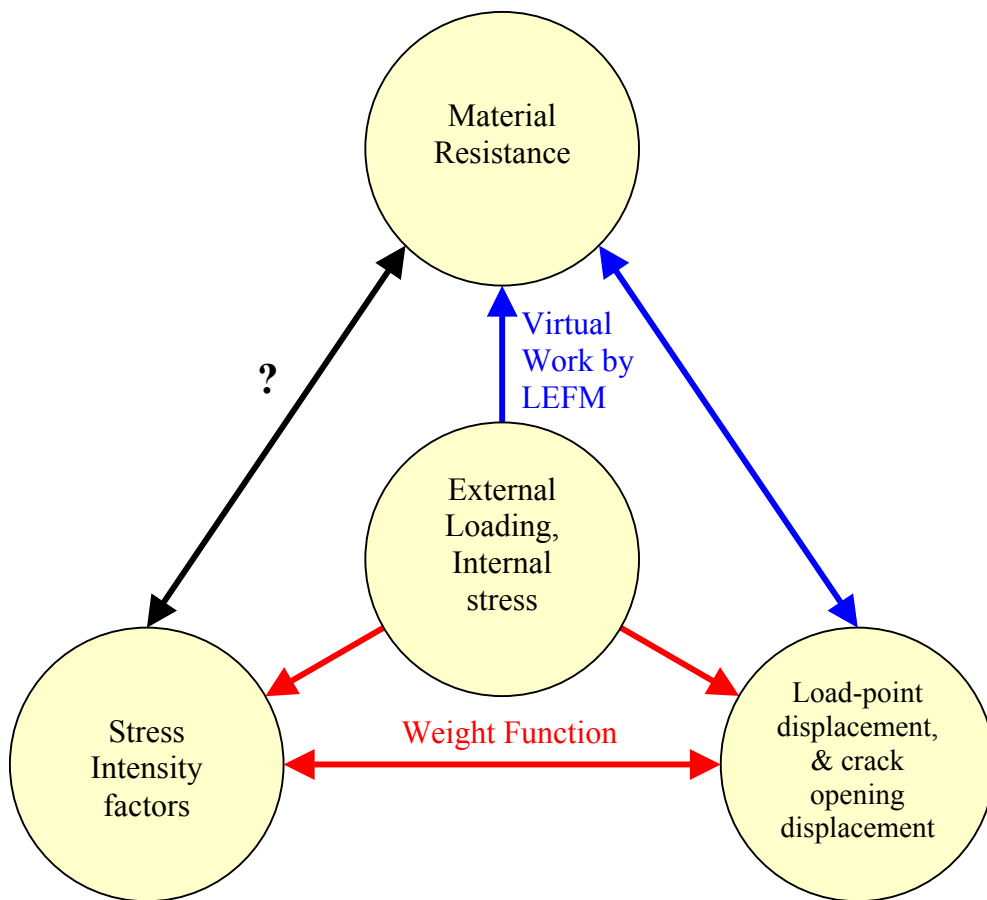


Fig. 3.3 The relationship among loading on boundary, the resultant displacements, the stress intensity factors and the material resistance in a quasi-static crack propagation process in linear elastic material. The loading, stress intensity factors, and the displacements are related by the weight function in LEFM; furthermore, the material resistance is derived from the virtual work calculated from the loading and the resultant displacements. However, the relationship between material resistance and the stress intensity factor is unknown.

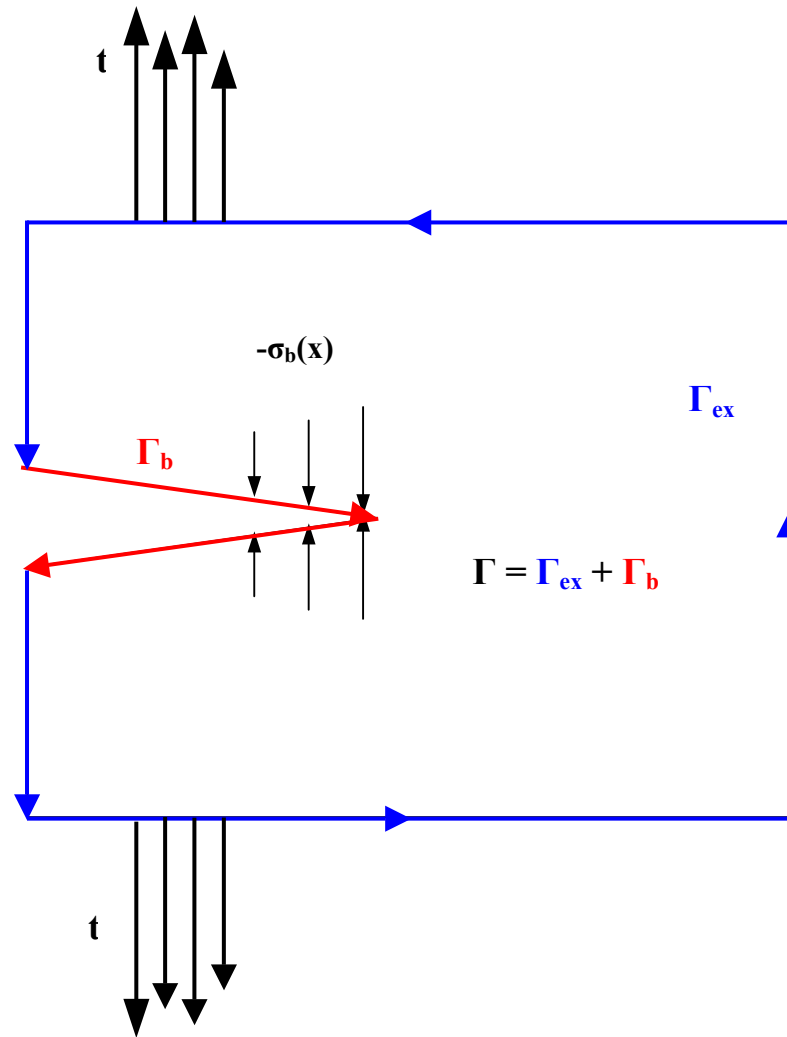
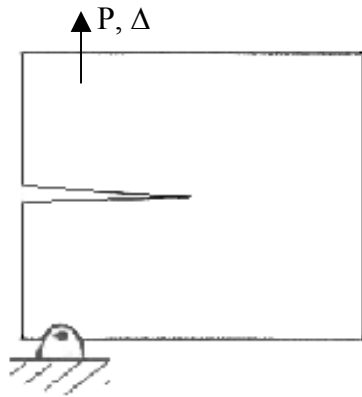
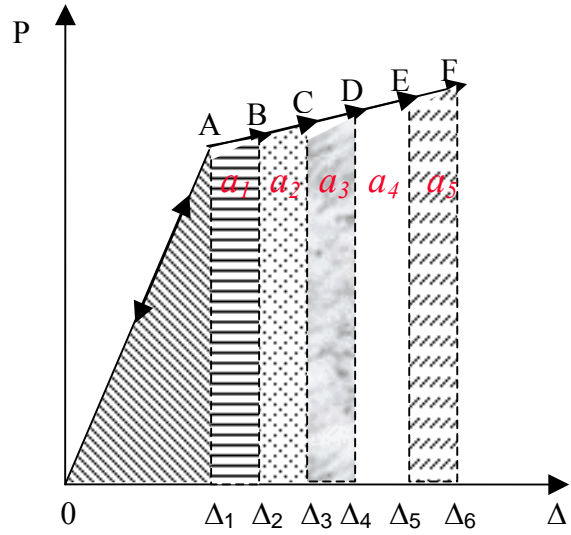


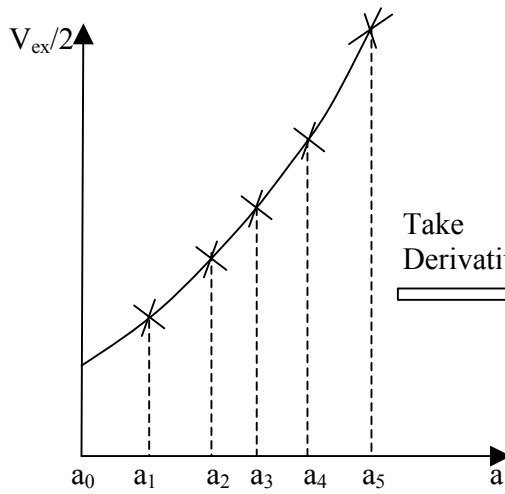
Fig. 3.4. Virtual work caused by external traction and internal compressive bridging stress is evaluated on the boundary of the specimen, where the crack faces are part of the boundary.



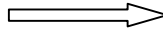
a) ASTM specimens

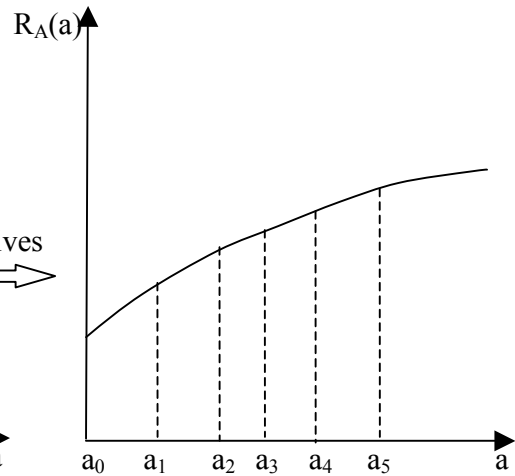


b) data collection from experiments: load, P , load point displacement, Δ , and crack length, a

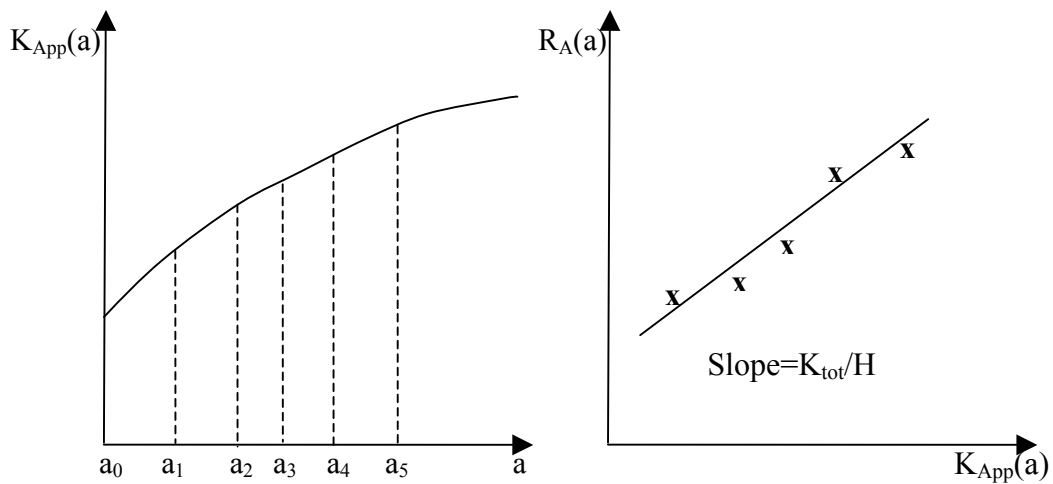


c) half of the virtual work vs. crack length a

Take Derivatives




d) Apparent fracture resistance vs. crack size a



e) applied stress intensity factor with crack length, a

f) Intrinsic stress intensity factor from the linear regression fit of $R_A(a)$ and $K_{App}(a)$

Fig. 3.5 Illustration of the experimental procedures to obtain the material resistance and the stress intensity factors. a) ASTM specimens; b) data collection from experiments: load, P , load-point displacement, Δ , and the crack size, a ; c) half of the virtual work vs. crack length a ; d) Apparent fracture resistance vs. crack size a ; e) applied stress intensity factor with crack length, a ; f) Intrinsic stress intensity factor from the linear regression fit of $R_A(a)$ and $K_{App}(a)$

Crack Opening Profiles

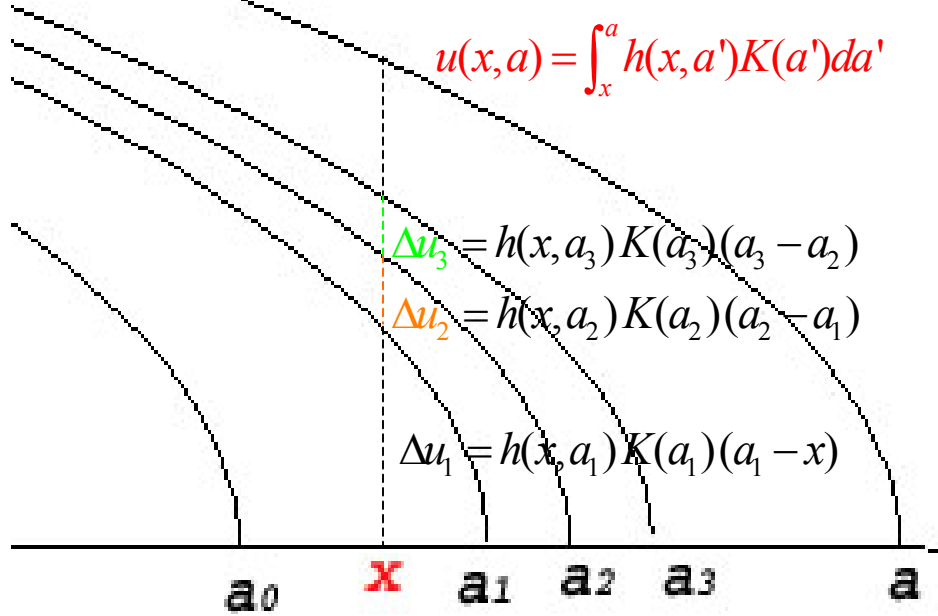


Fig. 3.6. Crack opening profiles with crack growth. When $a_0 \leq x$, there is no displacement at x ; when a passes x , the displacement increases with the crack length.

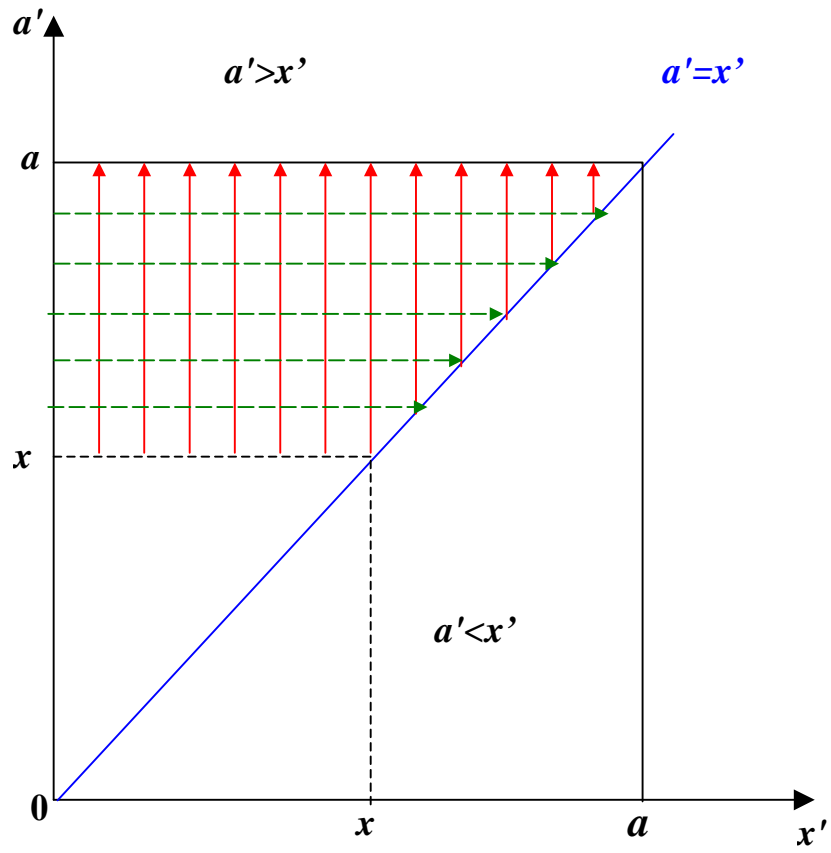


Fig. 3.7 Change of integral sequence to obtain the crack opening displacement from stress distribution along crack surfaces and weight functions. Broken arrows correspond to the integral sequence of the first equation in Eq. (A3.4) and solid ones to the sequence of the second equation in Eq. (A3.4).

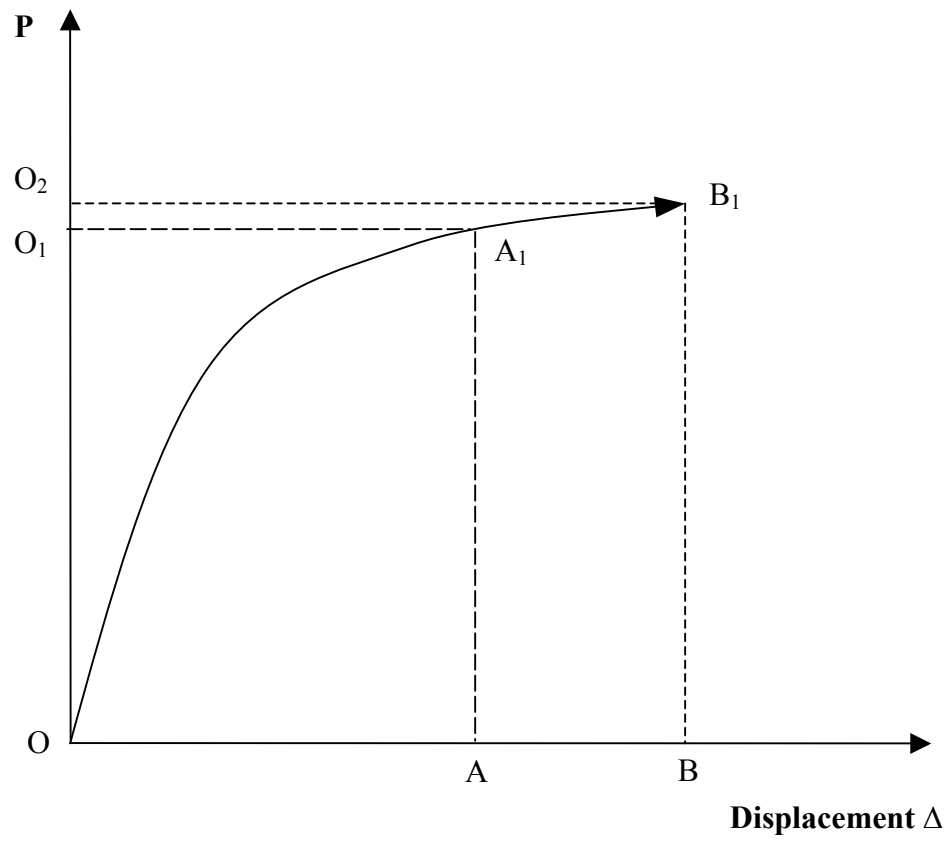
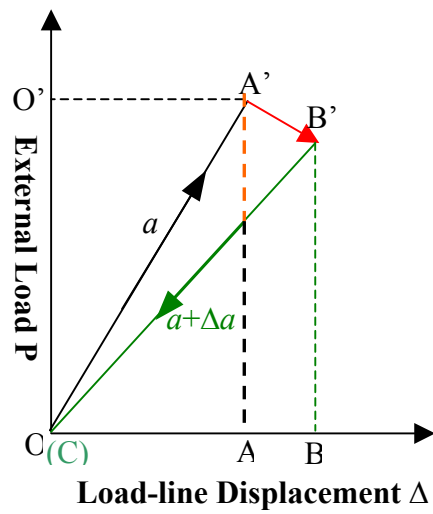
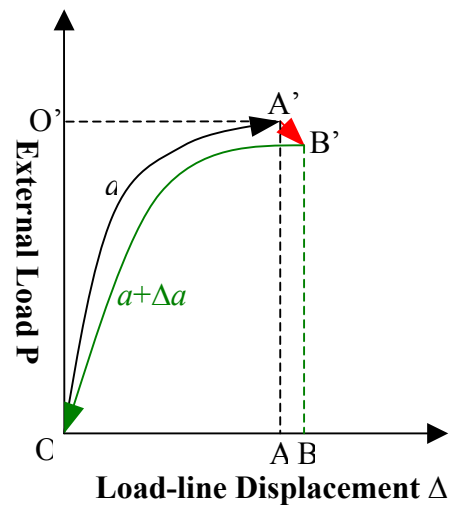


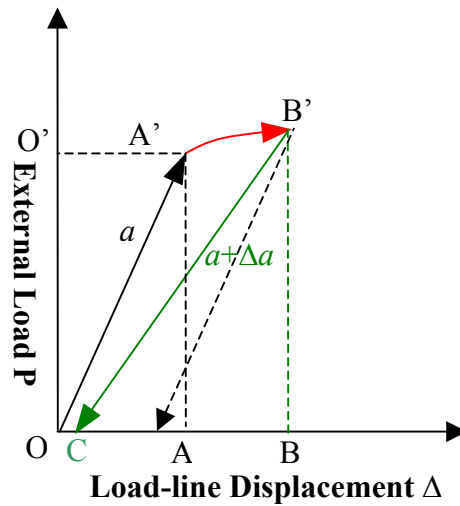
Fig. 3.8. At state 1, the actual work is the area OA_1A , virtual work OO_1A_1A ; at state 2, the actual work is the area OB_1B , virtual work OO_2B_1B .



a) linear elastic fracture



b) nonlinear elastic fracture



c) linear elastic-plastic fracture

Fig. 3.9 The incremental energy for crack growth from a to $a+\Delta a$ is indeed the loop of the work done $OA'B'C$, $c(B\Delta a)=\Delta W-\Delta U^{el}$. The equation holds true in elastically unloading materials experiencing a) linear elastic fracture; b) nonlinear elastic fracture; c) linear elastic-plastic fracture

CHAPTER 4

SUMMARY AND FUTURE WORK

An experimental study was made of a series of Al-containing silicon carbides (termed ABC-SiC) to examine the effect of microstructure on fracture and cyclic fatigue properties at both ambient and high temperatures. With the aluminum content increased from 3 to 5 to 7 wt% (3ABC, 5ABC and 7ABC-SiC), the toughening mechanism, and fracture and fatigue properties changed accordingly with the microstructure as follows:

- (1) *Microstructure.* Three microstructures were obtained as a result of adding different aluminum amounts. As the aluminum increases from 3 wt.% to 7wt.%, the grain structure varied from uniformly elongated to bimodal to equiaxed with a change in the nature of the grain-boundary film from amorphous to partially crystalline to fully crystalline.
- (2) *Fracture Property and Toughening Mechanism.* Of the three silicon carbides examined here (3, 5, and 7ABC-SiC), 5ABC-SiC demonstrated the highest peak toughness of $8.9 \text{ MPa}\sqrt{\text{m}}$ at 25°C and $7.1 \text{ MPa}\sqrt{\text{m}}$ at 1300°C . These high toughness values were attributed to crack-tip shielding, primarily from *uncracked-ligament* bridging in the crack wake. Corresponding toughening in 3ABC-SiC was primarily associated with *frictional* grain bridging; this structure displayed roughly 15% lower toughness. No bridging was detected in 7ABC microstructure, which accordingly exhibited the lowest toughness, comparable to that of commercial SiC.
- (3) *Cyclic Fatigue Properties and Mechanism.* Whereas the 7ABC structure was too brittle to be susceptible to fatigue, 3ABC and 5ABC exhibited cyclic

fatigue-crack growth at stress intensities above a $K_{\max,th}$ threshold which was roughly 80 – 90% of the peak toughness. Fatigue-crack growth in 3ABC and 5ABC was associated the suppression of crack bridging in the crack wake. In general, the 5ABC microstructure was less susceptible to fatigue, as evidenced by its steeper $da/dN-\Delta K$ curve. This was attributed to the higher resilience of uncracked-ligament bridging to degradation under cyclic loading, as compared to frictional grain bridging in 3ABC. While both the fracture toughness values and fatigue thresholds for 3 and 5ABC-SiC were found to be lower at 1300°C, the mechanisms of toughening and fatigue-crack propagation were found to be the same as at 25°C. No evidence of creep cavitation damage was detected during the fatigue testing at 1300°C.

In addition, an LEFM theoretical formulation was carried out for the expression between the fracture resistance and the stress intensity factors arising respectively from external load, internal compressive bridging stress, and intrinsic material resistance, and an experimental procedure was proposed to quantify above values from experimental data.

With respect to future work, the role of the nature of the grain boundaries in the transition of the bridging mechanisms from the frictional pullout in 3ABC to uncracked ligaments in 5ABC is not well understood. Neither known is the influence of the specimen size on the toughness increase associated with the internal bridging zone. Thus, the research listed below is still required to achieve a comprehensive understanding of the grain bridging mechanisms in non-transforming ceramics:

- (1) Chemical composition of the grain boundaries in ABC-SiCs should be examined using EDS, and the energy of grain boundary calculated from thermodynamics. With the values known of grain boundary energy, the

analysis for the local crack extension in a mixed mode (Mode I and Mode II) can be performed to quantify the role grain boundary energy in facilitating the formation of different bridging forms.

- (2) Commercial alumina should be used to study the effect of specimen size on the increase toughness because of its relatively good machinability. R-curve tests for the same material of different specimen sizes should be carried out, and the bridging zone length as well as CODs measured *in-situ* using the SEM. Comparison of the toughness values of the same material for different specimen sizes needs to be conducted in order to determine the critical specimen size above which the properties measured are broadly applicable to other structures.

With these studies a consistent description for the toughness of monolithic ceramics can be developed such that guidelines can be given for the design of new microstructures with optimum resistance to fracture and fatigue.